J|A|C|S ARTICLES

Published on Web 09/11/2009

Frustration of Magnetic and Ferroelectric Long-Range Order in $Bi_2Mn_{4/3}Ni_{2/3}O_6$

John B. Claridge,*,† Helen Hughes,† Craig A. Bridges,† Mathieu Allix,† Matthew R. Suchomel,† Hongjun Niu,† Xiaojun Kuang,† Matthew J. Rosseinsky,† Natalia Bellido,‡ Dominique Grebille,‡ Olivier Perez,‡ Charles Simon,‡ Denis Pelloquin,‡ Stephen J. Blundell,§ Tom Lancaster,§ Peter J. Baker,§ Francis L. Pratt,⊥ and P. Shiv Halasyamani¶

Department of Chemistry, University of Liverpool, Robert Robinson Laboratory, Crown Street Liverpool, Liverpool L69 7ZD, U.K., Laboratoire CRISMAT-ENSICAEN, UMR6508, 6 Bd du Maréchal Juin, 14050 Caen Cedex, France, Clarendon Laboratory, Department of Physics, Oxford University, Parks Road, Oxford OX1 3PU, U.K., ISIS Facility, Rutherford Appleton Laboratory, Chilton, Oxfordshire OX11 0QX, U.K., and Department of Chemistry, University of Houston, 136 Fleming Building, Houston, Texas 77204-5003

Received March 26, 2009; E-mail: j.b.claridge@liverpool.ac.uk

Abstract: The slight incommensurate modulation of the structure of $Bi_2Mn_{4/3}Ni_{2/3}O_6$ is sufficient to suppress the electrical polarization which arises in commensurate treatments of the structure, due to antiferroelectric coupling of local polar units of over 900 Å^3. The incommensurate structure is produced by the competition between ferroelectric Bi lone pair-driven A site displacement, chemical order of Mn and Ni on the B site, and both charge and orbital order at these transition metals. The interplay between the frustrated polar Bi displacements and the frustrated spin order at the B site, induced by positional disorder, produces magnetodielectric coupling between the incommensurately modulated lattice and the spin-glass-like ground state with an unusual relationship between the magnetocapacitance and the applied field.

Introduction

Multiferroic materials display two or more coexisting order parameters.[1] Multiferroics displaying long-range magnetic **M** and ferroelectric **P** order are of topical interest due both to candidate applications in multiple state memory storage and to the study of the physics behind the coupling of the two order parameters.[2−12] Multiferroic materials are created by the formation of composites of distinct ferromagnetic and ferroelectric phases,[13] or by the challenging task of identifying single phase materials with both properties.[14] Single phase materials typically have considerably weaker coupling between the magnetic and electric order, but are important as they can reveal the physical mechanism coupling **M** and **P**, or **M** and the relative permittivity ε_r. The search for single-phase materials displaying ferromagnetism and ferroelectricity is hampered by the conflicting electronic requirements of the two ground states - d^n centers are required for ferromagnetism but d^0 centers support the out-of-center distortions seen in classical ferroelectrics such as $BaTiO_3$.[14] The spatial separation of centers supporting the magnetization and the polarization is an attractive method of overcoming this problem and requires a complex crystal structure with distinct sites for the magnetically and electrically active ions. The ABO_3 perovskite meets this requirement as the A site can host ions with the ns^2 configuration which favors locally noncentric coordination (e.g Pb^{2+} in $PbTiO_3$) while the octahedral B site is occupied by transition metal cations bearing magnetic moments. $BiFeO_3$ is polar due to the asymmetric stereochemistry characteristic of Bi^{3+} on the A site, but has strong antiferromagnetic superexchange coupling of the d^5 Fe^{3+} centers. However, $BiFeO_3$ adopts a long period spiral magnetic structure with a small net moment[15,16] and it has been recently demonstrated that switching the polarization switches the

† University of Liverpool.
‡ Laboratoire CRISMAT-ENSICAEN, UMR6508.
§ Oxford University.
⊥ ISIS Facility, Rutherford Appleton Laboratory.
¶ University of Houston.

(1) Schmid, H. *Ferroelectrics* **1994**, *162*, 665–686.
(2) Nan, C.-W.; Bichurin, M. I.; Dong, S.; Viehland, D.; Srinivasan, G. *J. Appl. Phys.* **2008**, *103*, 031101/1−031101/35.
(3) Ramesh, R.; Spaldin, N. A. *Nat. Mater.* **2007**, *6*, 21–29.
(4) Cheong, S.-W.; Mostovoy, M. *Nat. Mater.* **2007**, *6*, 13–20.
(5) Ederer, C.; Spaldin, N. A. *Curr. Opin. Solid State Mater. Sci.* **2006**, *9*, 128–139.
(6) Eerenstein, W.; Mathur, N. D.; Scott, J. F. *Nature (London)* **2006**, *442*, 759–765.
(7) Spaldin, N. A.; Fiebig, M. *Science* **2005**, *309*, 391–392.
(8) Miao, L.; Song, G.; Wang, M.; Li, J. *Zhongguo Taoci Gongye* **2006**, *13*, 39–42.
(9) Chu, Y.-H.; Martin, L. W.; Holcomb, M. B.; Ramesh, R. *Mater. Today* **2007**, *10*, 16–23.
(10) Wakiya, N.; Shinozaki, K.; Kiguchi, T.; Yamada, T.; Mizutani, N. *Mater. Integr.* **2006**, *19*, 9–18.
(11) Khomskii, D. I. *J. Magn. Magn. Mater.* **2006**, *306*, 1–8.
(12) Prellier, W.; Singh, M. P.; Murugavel, P. *J. Phys.: Condens. Matter* **2005**, *17*, R803–R832.
(13) Zhai, J.; Xing, Z.; Dong, S.; Li, J.; Viehland, D. *J. Am. Ceram. Soc.* **2008**, *91*, 351–358.
(14) Hill, N. A. *J. Phys. Chem. B* **2000**, *104*, 6694–6709.
(15) Kubel, F.; Schmid, H. *Acta Crystallogr., Sect. B* **1990**, *46*, 698–702.

10.1021/ja902424x CCC: $40.75

helicity.[17] $BiMnO_3$[18−22] is an insulating ferromagnet due to orbital ordering at the Mn^{3+} center with a controversial crystal structure whose polar nature appears to depend on the length scale of the probe used.[23−25] There is also some controversy as to the exact composition.[26,27]

The combination of the asymmetric stereochemistry characteristic of Bi^{3+} on the perovskite A site with multiple B site cations allows the use of the Goodenough−Kanamori rules to design target systems where ferromagnetic exchange is expected. Site-ordered Bi_2FeCrO_6[28] is predicted to be ferrimagnetic, but bulk materials[29] are spin glasses due to the absence of long-range cation order, though some progress has been made in the area of artificial superlattices.[30,31] The electronic prerequisite for ferromagnetic coupling in an insulator is that partially filled orbitals interact with filled or empty ones, so the expected ferromagnetic exchange coupling between e_g^0 Mn^{4+} and e_g^2 Ni^{2+} makes Bi_2MnNiO_6 an attractive synthetic target. This material is accessible by high-pressure synthesis.[32] We showed that ambient pressure synthesis at this composition affords instead the Mn-rich phase $Bi_2Mn_{4/3}Ni_{2/3}O_6$,[33] which is unusual as one of only four examples (the others are $BiFeO_3$,[15,34] which can be doped on the B site to a limited extent, and $Bi_2M_{3/4}Fe_{1/2}Ti_{3/4}O_6$ (M = Mg, Ni)[35]) of a perovskite stable under ambient pressure synthesis conditions with occupation of the A site solely by Bi^{3+}; most Bi^{3+} perovskites require high-pressure synthesis due to the mismatch of this small cation with the 12-coordinate A site. Laboratory X-ray and electron diffraction studies reveal a large commensurate unit cell which appears polar, consistent with a phase transition apparent in relative permittivity measurements. Here we show with high angular resolution synchrotron powder diffraction data that the ambient-temperature structure of $Bi_2Mn_{4/3}Ni_{2/3}O_6$ is incommensurately modulated and present an analysis of the structure using the appropriate five-dimensional treatment of the structure. This reveals that the incommensurate modulation results in cancellation of the polarization in the individual commensurate unit cells to make the system nonpolar over the length scale of the modulation. The competing magnetic interactions which arise from the distribution of cations and charge states on the B site produce a spin-glass-like rather than ferromagnetic magnetic ground state. Despite this suppression of both magnetic and electrical orders, there is significant magnetocapacitance below the spin-glass freezing temperature.

Experimental Section

Synthesis. $Bi_2Mn_{4/3}Ni_{2/3}O_6$ samples were prepared by a standard ceramic method, on a scale between 0.5 g and 5 g. Stoichiometric quantities of Bi_2O_3 (Alfa 99.9995%), MnO_2 (Alfa Aesar 99.999%), and NiO (Alfa Aesar 99.998%) were ground together in a ball mill with Mg-stabilized zirconia milling media for 12 h and pelletized. The pellet was placed on platinum foil in an alumina boat (reaction occurs with the boat if this precaution is not taken) and heated at 800 °C for 12 h, 850 °C for 12 h, and then 875 °C for 12 h. The pellet was ground in an agate mortar and pestle, repelletized, and heated at 850 °C for 12 h. This process was repeated twice. All steps used a heating rate of 5 °C per minute and a cooling rate of 10 °C per minute.

Oxygen content was determined by chemical analysis using redox titration. The sample was first dissolved in 6 M HCl solution under an argon atmosphere: an excess of KI was then added to reduce the manganese and nickel species to Mn^{2+} and Ni^{2+}. The I_2 formed was then titrated using sodium thiosulfate in order to work out the quantity of reduced cations. This value then leads to the oxygen content assuming bismuth is in the +III oxidation state.

Crystal Growth. A number of attempts were made to grow crystals of $Bi_2Mn_{4/3}Ni_{2/3}O_6$. Bi_2O_3:NaCl[36] and Bi_2O_3:B_2O_3[15] fluxes were selected as they had been previously used to grow crystals of $BiFeO_3$. However, only the Bi_2O_3:NaCl flux was found to form crystals of $Bi_2Mn_{4/3}Ni_{2/3}O_6$. A range of different temperatures, dwell times, heating and cooling rates were attempted along with a range of flux compositions and masses in order to maximize the yield of crystals formed. The most successful flux conditions are detailed below.

The starting composition consisted of Bi_2O_3 (64.12 mol %), MnO_2 (20.24 mol %), NiO (10.12 mol %), and NaCl (5.52 mol %) with a total mass of 30 grams. The mixture was heated in a platinum crucible (14 mL volume) covered with a lid at 800 °C for 12 h, then 850 °C for 12 h, then 875 °C for 3 h at a rate of 5 °C/minute. The flux was then slow cooled to 820 °C at a rate of 0.5 °C/hour, then finally cooled to room temperature at a rate of 5 °C/minute. The crystals were removed from the flux by boiling the mixture in 4 M HNO_3 for approximately four days, followed by filtering. The crystals obtained were cubic in shape and approximately 1 mm per edge in size. These crystals were used for the measurements described below, with the synchrotron powder diffraction data being collected on a ground set of single crystals.

Neutron Powder Diffraction. Powder diffraction data was collected on the D2b diffractometer at the ILL at 5K and 300K (λ = 1.59452(3) Å), and on the GEM diffractometers at ISIS between

(16) Popov, Y. F.; Kadomtseva, A. M.; Zvezdin, A. K.; Vorob'ev, G. P.; Pyatakov, A. P. *NATO Science Series, II: Mathematics, Physics and Chemistry*; Springer; Dordrecht, The Netherlands, 2004; Vol. 164, pp 277−290.
(17) Lebeugle, D.; Colson, D.; Forget, A.; Viret, M.; Bataille, A. M.; Gukasov, A. *Phys. Rev. Lett.* **2008**, *100*, 227602.
(18) Chi, Z. H.; Yang, H.; Feng, S. M.; Li, F. Y.; Yu, R. C.; Jin, C. Q. *J. Magn. Magn. Mater.* **2007**, *310*, e358−e360.
(19) Moreira dos Santos, A.; Cheetham, A. K.; Atou, T.; Syono, Y.; Yamaguchi, Y.; Ohoyama, K.; Chiba, H.; Rao, C. N. R. *Phys. Rev. B* **2002**, *66*, 064425/1−064425/4.
(20) Atou, T.; Chiba, H.; Ohoyama, K.; Yamaguchi, Y.; Syono, Y. *J. Solid State Chem.* **1999**, *145*, 639–642.
(21) Sugawara, F.; Iida, S.; Shono, Y.; Akimoto, S. *J. Phys. Soc. Jpn.* **1965**, *20*, 1529.
(22) Kimura, T.; Kawamoto, S.; Yamada, I.; Azuma, M.; Takano, M.; Tokura, Y. *Phys. Rev. B* **2003**, *67*, 4.
(23) Kodama, K.; Iikubo, S.; Shamoto, S.-i.; Belik, A. A.; Takayama-Muromachi, E. *J. Phys. Soc. Jpn.* **2007**, *76*, 124605/1–124605/7.
(24) Yokosawa, T.; Belik, A. A.; Asaka, T.; Kimoto, K.; Takayama-Muromachi, E.; Matsui, Y. *Phys. Rev. B: Condens. Mater. Phys.* **2008**, *77*, 024111/1−024111/7.
(25) Montanari, E.; Calestani, G.; Righi, L.; Gilioli, E.; Bolzoni, F.; Knight, K. S.; Radaelli, P. G. *Phys. Rev. B* **2007**, *75*, 220101/1–220101/4.
(26) Belik, A. A.; Kolodiazhnyi, T.; Kosuda, K.; Takayama-Muromachi, E. *J. Mater. Chem.* **2009**, *19*, 1593–1600.
(27) Sundaresan, A.; Mangalam, R. V. K.; Iyo, A.; Tanaka, Y.; Rao, C. N. R. *J. Mater. Chem.* **2008**, *18*, 2191–2193.
(28) Baettig, P.; Ederer, C.; Spaldin, N. A. *Phys. Rev. B* **2005**, *72*, 8.
(29) Suchomel, M. R.; Thomas, C. I.; Allix, M.; Rosseinsky, M. J.; Fogg, A. M.; Thomas, M. F. *Appl. Phys. Lett.* **2007**, *90*.
(30) Nechache, R.; Carignan, L. P.; Gunawan, L.; Harnagea, C.; Botton, G. A.; Menard, D.; Pignolet, A. *J. Mater. Res.* **2007**, *22*, 2102–2110.
(31) Ichikawa, N.; Arai, M.; Imai, Y.; Hagiwara, K.; Sakama, H.; Azuma, M.; Shimakawa, Y.; Takano, M.; Kotaka, Y.; Yonetani, M.; Fujisawa, H.; Shimizu, M.; Ishikawa, K.; Cho, Y. *Appl. Phys. Express* **2008**, *1*, 3.
(32) Azuma, M.; Takata, K.; Saito, T.; Ishiwata, S.; Shimakawa, Y.; Takano, M. *J. Am. Chem. Soc.* **2005**, *127*, 8889–8892.
(33) Hughes, H.; Allix, M. M. B.; Bridges, C. A.; Claridge, J. B.; Kuang, X. J.; Niu, H. J.; Taylor, S.; Song, W. H.; Rosseinsky, M. J. *J. Am. Chem. Soc.* **2005**, *127*, 13790–13791.
(34) Royen, P.; Swars, K. *Angew. Chem.* **1957**, *69*, 779.
(35) Bridges, C. A.; Allix, M.; Suchomel, M. R.; Kuang, X.; Sterianou, I.; Sinclair, D. C.; Rosseinsky, M. J. *Angew. Chem., Int. Ed.* **2007**, *46*, 8785–8789.
(36) Gabbasova, Z. V.; Kuzmin, M. D.; Zvezdin, A. K.; Dubenko, I. S.; Murashov, V. A.; Rakov, D. N.; Krynetsky, I. B. *Phys. Lett. A* **1991**, *158*, 491–498.

5 and 550 K. Rietveld refinements were carried using JANA2006[37−39] on the D2b data using a 15 term Legendre polynomial for the background and the pseudo-Voigt peak shape. Bismuth positions were freely refined; however, the transition metal and oxygen sites were refined such that the Mn/Ni−O distances were restrained to be in the range 2.0(±0.3) Å. Anisotropic displacement parameters were refined for Bi and O, and isotropic displacement parameters for all atoms were refined. Further details of the refinement are given in the Results section.

Single Crystal X-ray Diffraction. The single crystal X-ray diffraction study was performed at room temperature using Mo Kα radiation with a Bruker Kappa CCD diffractometer. A first cell was determined using reflections with $\theta < 30°$. Given the obvious twinning the data were collected in the orthorhombic system: $a = 15.60$ Å, $b = 15.52$ Å, $c = 15.61$ Å. Data collection was performed using $\varphi-\omega$ scans with $0° < \theta < 45°$, with steps of 0.3°/frame and a sample detector distance of 34 mm. Data reduction and integration was performed using the EVALCCD software.[40] Absorption corrections were applied using the SADABS program.[41] Structure refinement was performed using the JANA2006 software package.[38] Anisotropic displacement parameters were refined for Bi and an isotropic displacement parameter for Mn/Ni was refined, oxygen thermal parameters were fixed at 0.01 Å^2. Peaks with $m, n \leq 2$ were included in the refinement, and atomic displacements up to second order were refined for all atoms; first-order terms were refined for the Bi anisotropic thermal parameters.

X-ray Powder Diffraction. X-ray powder diffraction data were collected on station 9.1 of the Daresbury Synchrotron Radiation Source between room temperature and 450 °C on both the $Bi_2Mn_{4/3}Ni_{2/3}O_6$ ceramic sample and a sample of ground flux grown crystals. During heating data was collected over a small 2θ range, allowing the cell parameters to be tracked as a function of temperature. Data were refined by the Rietveld method using the JANA2006 software package.[37,39]

Transmission Electron Microscopy. Samples for transmission electron microscopy were prepared by crushing the powder in *n*-butanol, and the small crystallites in suspension were deposited onto a holey carbon film, supported by a copper grid. The electron diffraction (ED) study was carried out with a JEOL 2000FX at room temperature and a JEOL 2010 for the temperature-dependent study. High-resolution electron microscopy (HREM) was performed using a TOPCON 002B microscope operating at 200 kV and having a point resolution of 1.8 Å. Energy dispersive spectroscopy (EDS) analyses were systematically carried out during the study, all microscopes being equipped with an EDAX analyzer.

Magnetic Measurements. Magnetic susceptibility data were collected using a Quantum Design MPMS SQUID magnetometer. Each sample was loaded at room temperature and cooled in the absence of an applied field to 2 K. A field of 100 Oe was then applied, and measurements were recorded between 2 and 300 K; this system was then cooled again to 2 K in the applied field, and the measurements between 2 and 300 K were repeated.

dc Magnetization hysteresis loops were recorded with a field sweep between ± 5.5T at 2, 25, 60, and 300 K. A maximum magnetic moment of 3.55 μ_B/mol was observed in the 2 K data, however saturation of the sample was not achieved by a field of ± 5.5T.

ac Susceptibility data was recorded over a 1−1000 Hz frequency range with an ac driving field of 1 Oe. The frequency dependency of the maxima in the susceptibility data indicated that the transition at 35 K was due to spin-glass freezing rather than long-range magnetic ordering. This was confirmed by the displaced nature of a dc magnetization hysteresis loop (field sweep between ±1 T) that was recorded on the crystal sample at 2 K after cooling from 300 K in a field of 1T.

All measurements were carried out on both the ceramic and crystal $Bi_2Mn_{4/3}Ni_{2/3}O_6$ samples. However, the data obtained from the crystal sample were regarded as the most accurate as the crystal sample contained the least amount of trace impurities; as a result all figures quoted have been calculated from the crystal data set. All samples were measured inside a gelatin capsule that was fixed to the midpoint of a straw. Ceramic samples were measured in the form of pressed pellets that were fixed into place by inverting the capsule. Crystals were measured in the same way; however, they were held in place using vacuum grease to prevent them spinning in the applied field.

Muon Spin Relaxation. Zero-field muon spin relaxation (ZF-μ^+SR) measurements were made on a powder sample of $Bi_2Mn_{4/3}Ni_{2/3}O_6$ using the μ^+SR instrument at the ISIS Pulsed Muon facility, Rutherford Appleton Laboratory, U.K., using a closed-cycle refrigerator. The samples were wrapped in silver foil and mounted on a silver sample holder. In a μ^+SR experiment[42] spin-polarized positive muons are stopped in a target sample, where the muon usually occupies an interstitial position in the crystal. The observed property in the experiment is the time evolution of the muon spin polarization, the behavior of which depends on the local magnetic field at the muon site. Each muon decays, with a lifetime of 2.2 μs, into two neutrinos and a positron, the latter particle being emitted preferentially along the instantaneous direction of the muon spin. Recording the time dependence of the positron emission directions therefore allows determination of the spin polarization of the ensemble of muons. In our experiments, positrons are detected by detectors placed forward (F) and backward (B) of the initial muon polarization direction. Histograms $N_F(t)$ and $N_B(t)$ record the number of positrons detected in the two detectors as a function of time following the muon implantation. The quantity of interest is the decay positron asymmetry function that is defined as

$$A(t) = (N_F(t) - \alpha N_B(t))/(N_F(t) + \alpha N_B(t)),$$

where α is an experimental calibration constant. $A(t)$ is proportional to the spin polarization of the muon ensemble.

X-ray Absorption Spectroscopy (XAS). XAS was carried out on station 7.1 at the SRS. Data were recorded on samples at room temperature across the Mn and Ni K edge in ∼0.5 eV steps, Mn and Ni metal K edges were run simultaneously as an energy calibration. All samples were recorded in transmission mode, $BiMnO_3$, $LaMnO_3$, $CaMnO_3$, La_2MnNiO_6, La_2NiO_4, and $LaSrNiO_4$ were all run as Mn^{3+}, Mn^{4+}, Ni^{2+}, and Ni^{3+} standards, respectively.

Magnetoelectric Measurements. Two parallel surfaces of a single crystalline sample of dimensions 0.51 mm × 0.58 mm × 0.59 mm were covered with silver paste in order to create a capacitor, and two coaxial cables were contacted to each surface. A homemade sample holder allows the system to be placed in the sample space of a Quantum Design PPMS system, where temperature and magnetic field can be controlled. This system allows the measurement of the complex impedance of the sample under a magnetic field with an Agilent 4284A LCR-meter. Measurements have been done applying an ac voltage of 1 V amplitude at a frequency of 100 kHz. At low temperatures the sample has a dielectric loss small enough to model it as a resistance and a capacitor in parallel; the relative permittivity is obtained (ε) from this capacitance value, taking into account geometrical factors. The magnetodielectric effect is defined by its relative permittivity in eq 1:

(37) Petricek, V.; Dusek, M.; Palatinus, L. *Jana2006*. The crystallographic computing system; Institute of Physics: Praha, Czech Republic, 2006.
(38) Petricek, V.; Dusek, M. *Z. Kristallogr.* **2004**, *219*, 692–700.
(39) Dusek, M.; Petricek, V.; Wunschel, M.; Dinnebier, R. E.; van Smaalen, S. *J. Appl. Crystallogr.* **2001**, *34*, 398–404.
(40) Duisenberg, A. J. M.; Kroon-Batenburg, L. M. J.; Schreurs, A. M. M. *J. Appl. Crystallogr.* **2003**, *36*, 220–229.
(41) Sheldrick, G. M. *SADABS*; University of Göttingen: Göttingen, Germany, 1997.
(42) Blundell, S. J. *Contemp. Phys.* **1999**, *40*, 175–192.

$$\Delta\varepsilon_H/\varepsilon_0 = \frac{\varepsilon(H) - \varepsilon(H=0T)}{\varepsilon(H=0T)} \times 100 \qquad (1)$$

The relative permittivity measures the electrical polarizability of the sample so that if some coupling exists between magnetic ordering and the local electrical polarization, the relative permittivity should show anomalies at the temperature of magnetic order and/or a clear dependence on the applied magnetic field H.

Optical Measurements. Powder second harmonic generation (SHG) was performed on a modified Kurtz-NLO system[43] using a pulsed Nd:YAG laser with a wavelength of 1064 nm. A detailed description of the equipment and methodology has been published.[44] No index matching fluid was used in any of the experiments.

Results

Room-Temperature Structure. Solid-state synthesis at the $Bi_2Mn_{4/3}Ni_{2/3}O_6$ composition produces single-phase material at this composition under the conditions described in the Experimental Section.

Reciprocal space reconstructions were performed for characteristic crystallites from electron diffraction (ED) patterns by tilting around the crystallographic axes. Careful examination of the principal axis electron diffraction patterns presented in Figure S1 reveals the coexistence of quite intense and relatively weak reflections. This feature is in agreement with the coexistence of different periodicities and is then characteristic of a modulated structure.

With the reciprocal space resolution of electron diffraction, this modulation appears commensurate,[33] so that we first studied this compound as a superstructure. The analysis of the ED patterns on Figure S1 shows that this new phase is related to the perovskite structure: the system of reflections gives a tetragonal cell with $a \approx \sqrt{2}a_p$, $b \approx 2\sqrt{2}a_p$, and $c \approx 4a_p$ (a_p being the parameter of the cubic perovskite-type structure). No condition limiting the general *hkl* reflections was observed, involving a P lattice while the only extra condition, 0*kl*: $k + l = 2n$ implying a *n* glide along *a*, restrained us to one of the three following space groups: *Pnmm*, $Pnm2_1$ and $Pn2_1m$ and possibly *Pn*11 or *P*2/*n*11 (with $\alpha \sim 90°$).

Two sets of single crystal X-ray data were investigated; the first collected at the SRS on beamline 9.8 and the second using laboratory radiation. Both data sets suffered from significant microtwinning as would be expected as there is at least one structural transition between room temperature and the synthesis temperature (see below); therefore, the second data set was collected in a pseudo-cubic $4a_p \times 4a_p \times 4a_p$ cell which indexes all six possible symmetry related orientations of the $\sqrt{2}a_p \times 2\sqrt{2}a_p \times 4a_p$ cell relative to the original cubic perovskite axes. Examination of the data indicated two dominant domains related by interchanging **a** and **b**, however attempts to index the entire pattern using only two domains always omitted a significant number of peaks. Refinements of both data sets, based on the initial crystal refinement,[33] reinforced the conclusion that the $\sqrt{2}a_p \times 2\sqrt{2}a_p \times 4a_p$ structure is best described in the polar space group $Pnm2_1$. HREM lattice images of the room-temperature modulated structure are clearly related to a perovskite-type structure - examination of the local variations of contrast in the thicker part of the crystal is consistent with the supercell model (Figure 1).

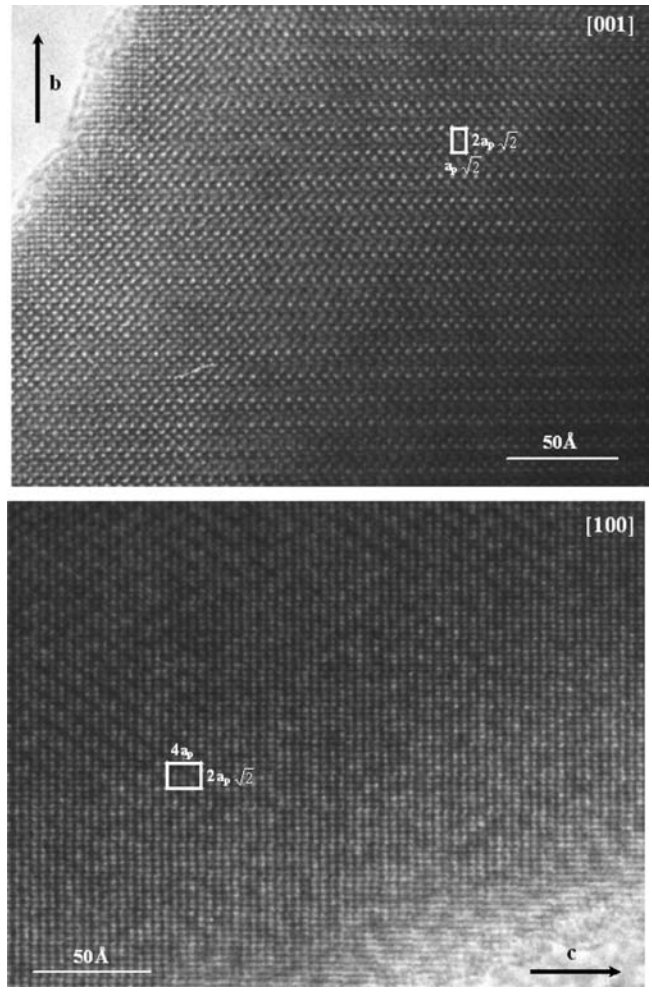

Figure 1. Experimental HREM image of $Bi_2Mn_{4/3}Ni_{2/3}O_6$ recorded at room temperature along the [001] and [100] directions and indexed in the commensurate supercell setting.

However, attempts to fit the high resolution synchrotron powder data showed systematic misfits to reflections with *hkl*: *h*, $k = 2n+1$ (Figure 2a), (note that here we have transformed the cell from the **abc** setting above to the **bca** setting for convenience in the later discussion). Attempts to account for this via a monoclinic distortion led to unstable refinements. In all of the single crystal XRD, SAED and powder XRD data, the strongest peaks belong to a $\sqrt{2}a_p \times 2a_p \times \sqrt{2}a_p$ cell and have $h+k+l = 2n$. Given the previously observed modulations in $Bi_{1-x}Sr_xMnO_3$[45,46] it was decided to explore a modulated description of the structure. The interest of such a superspace approach even in commensurate cases is shown in the structural studies of $Bi_{1-x}Ca_xMnO_3$ ($x = 0.4$ and 0.45).[47] Reindexing SAED and single crystal XRD data was achieved with an Ibmm $\sqrt{2}a_p \times 2a_p \times \sqrt{2}a_p$ sub cell and two modulation vectors $\mathbf{p}^* = \alpha\mathbf{a}^*$ and $\mathbf{q}^* = -\beta\mathbf{b}^*$ ($\alpha,\beta \sim 1/2$) In this setting the observed absences correspond to *hklmn:* $h+k+l = 2n$, *hk*0*mn:* $m + n = 2n$ and 0*klmn:* $k = 2n$, where *m* and *n* correspond to the directions defined by $\mathbf{p}^*$ and $\mathbf{q}^*$. (Figure 3).

(43) Kurtz, S. K.; Perry, T. T. *J. Appl. Phys.* **1968**, *39*, 3798.
(44) Ok, K. M.; Chi, E. O.; Halasyamani, P. S. *Chem. Soc. Rev.* **2006**, *35*, 710–717.
(45) Frontera, C.; Garcia-Munoz, J. L.; Aranda, M. A. G.; Hervieu, M.; Ritter, C.; Manosa, L.; Capdevila, X. G.; Calleja, A. *Phys. Rev. B* **2003**, *68*, 134408/1–134408/8.
(46) Hervieu, M.; Malo, S.; Perez, O.; Beran, P.; Martin, C.; Baldinozzi, G.; Raveau, B. *Chem. Mater.* **2003**, *15*, 523–527.
(47) Giot, M.; Pautrat, A.; Perez, O.; Simon, C.; Nevriva, M.; Hervieu, M. *Solid State Sci.* **2006**, *8*, 1414–1421.

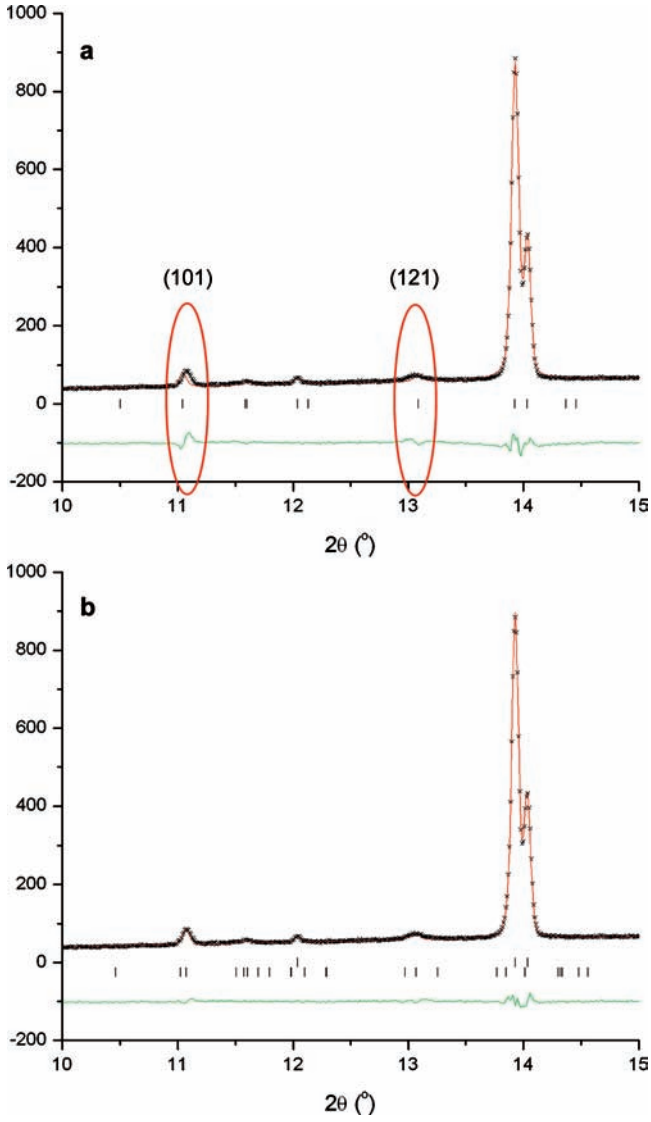

Figure 2. Low angle region of a Le Bail extraction of the room temperature synchrotron XRD data from the ground single crystal sample of $Bi_2Mn_{4/3}Ni_{2/3}O_6$ in (a) $P2_1mn$ ($2\sqrt{2}a_p \times 4a_p \times \sqrt{2}a_p$), showing the positional mismatch for peaks with *hkl: h, k = 2n+1*. (b) using the superspace formalism ($\alpha = 0.4925(2)$, $\beta = 0.4799(7)$). Crosses are observed data, the solid red line is the calculated pattern, and the green line is the difference. In (b) the upper tick marks correspond to the positions of the subcell Bragg peaks, and the lower ones to the incommensurate satellite reflections.

In order to obtain these reflection conditions, the following generators were used with I centering (1/2,1/2,1/2,0,0):

$$x,\ y,\ z,\ t,\ u$$

$$-x,\ 1/2 + y,\ z, 1/2 - t,\ u$$

$$x,\ 1/2 - y,\ z,\ t,\ 1/2 - \mathrm{u}$$

$$-x,\ -y,\ z,\ 1/2 - t,\ 1/2 - u$$

The superspace group is then *Ibmm(α00,0−β0)mm.ss*.

Owing to the periodicity in superspace[48,49] each parameter of the modulated structure (i.e., *x*,*y*,*z*, U_{ij}) can be expressed in terms of a Fourier series (for the μth parameter, eq 2):

$$p^{\mu}(x_4, x_5) = \sum_n \sum_m [p^{\mu}_{snm} \sin(2\pi n x_4 + 2\pi m x_5) + p^{\mu}_{cnm} \cos(2\pi n x_4 + 2\pi m x_5)] \quad (2)$$

where $x_4 = q_1 r^{\mu} + t$, $x_5 = q_2 r^{\mu} + u$; t and u are the internal phases and p^{μ}_{snm} is the sine term corresponding to modulation

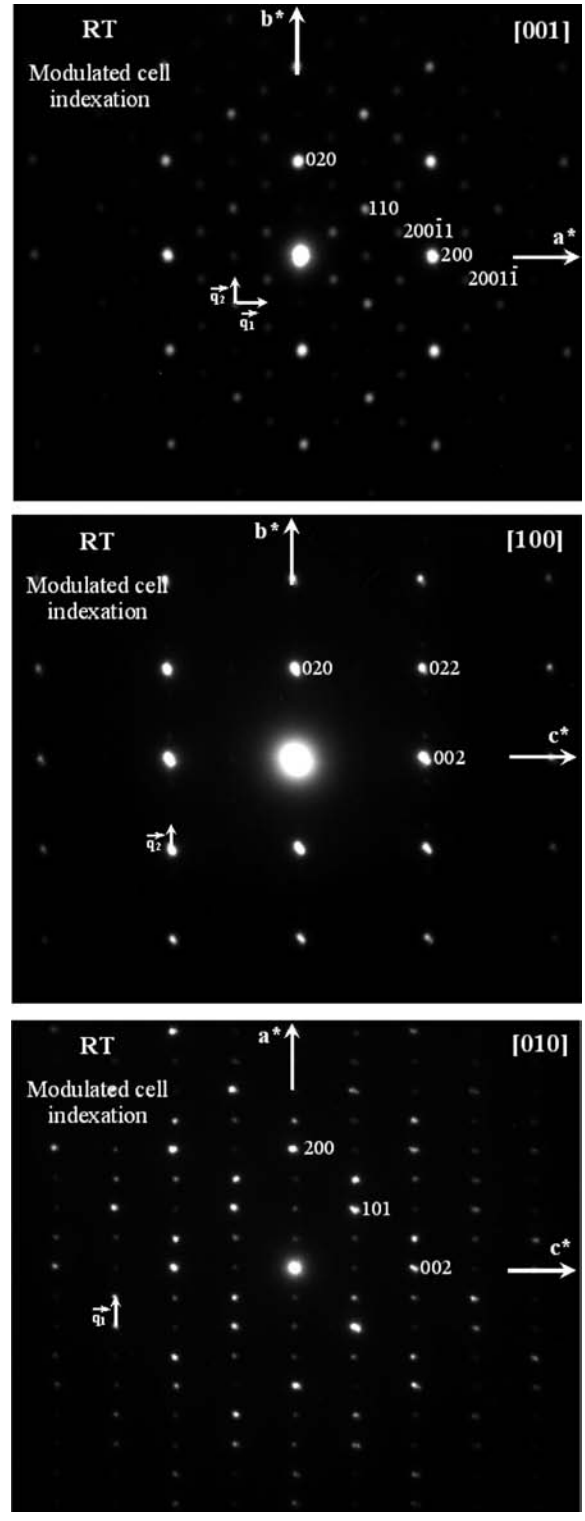

Figure 3. Experimental electron diffraction patterns recorded at room temperature along the [100], [010], and [001] directions and indexed using the incommensurate modulated setting. The data show that the modulation is in the *ab* plane.

(48) Janner, A.; Janssen, T. *Phys. Rev. B* **1977**, *15*, 643–658.
(49) Yamamoto, A. *Acta Crystallogr., Sect. A* **1996**, *52*, 509–560.

Table 1. Possible Superstructure Spacegroups for $Bi_2Mn_{4/3}Ni_{2/3}O_6$, for $\alpha,\beta = 1/2$ As a Function of the Origin (t,u) in Superspace

	$t = (2n+1)/8$	$t = (2n)/8$	$t =$ other
$u = (2n+1)/8$	$Pcmn$	$P2_1mn$	$P2_1mn$
$u = (2n)/8$	$Pc2_1n$	$P112/n$	$P11n$
$u =$ other	$Pc2_1n$	$P11n$	$P11n$

wave nm of parameter μ. The Q-resolution of both the single crystal diffractometers in the geometries used for data collection here and of the SAED is insufficient to permit the exact determination of α and β, which are 1/2 within experimental error. An accurate analysis of the α and β values will be proposed later. However, in a first approximation, commensurate values are assumed ($\alpha,\beta = 1/2$) for the structural determination. The case $\alpha,\beta = 1/2$ lead to possible overlap of main and satellite reflections; the use of the commensurate option permits this problem to be dealt with. But, since additional reflection overlaps due to twinning occur, the treatment of domains is added to the usual complexity of solving a modulated phase. In this framework, working out a reliable solution is difficult, because an accurate separation of the diffracted intensities from different domains is challenging and the effects of coherence and antiphase boundaries are hard to model.

In the commensurate case the different sections of the super crystal, defined by different values of the origin in superspace (u, t correspond to the origins in the two new dimensions), are not equivalent, since only one will describe the actual three-dimensional commensurate structure. The possible sections and their symmetry are listed in Table 1. For refinements, four modulation waves were considered for each parameter in accordance with the following vector combination $\mathbf{p}$, $\mathbf{q}$, $\mathbf{p} + \mathbf{q}$ and $\mathbf{p} - \mathbf{q}$. Refinements equivalent to the supercell structure reported previously ($t = 1/4$, $u = 1/8$ and $t = 1/4$, $u = 3/8$ equivalent to $P2_1mn$, $R_{obs} = 7.97\%$) gave the best fits (refinements equivalent to $P11n$ ($t = 1/4$, $u = 0.167$ chosen as an arbitrary value, $R_{obs} = 8.31\%$) were only slightly worse) the observation that three distinct polar structures fit the commensurately analyzed data is consistent with the need for an incommensurate refinement. The use of centrosymmetric origins ($t = 1/4$, $u = 1/2$ equivalent to $P112/n$, $R_{obs} = 10.43\%$ and $t = 1/8$, $u = 1/8$ equivalent to $Pcmn$, $R_{obs} = 18.81\%$) gives worse fits. Conventional nonmodulated refinements in $P2_1mn$ gave $R_{obs} = 7.94\%$, significantly though using 101 rather than 88 structural parameters. It should be noted that second order terms are necessary to generate polar structures in the commensurate case as single sine and cosine terms always yield centric structures due to the superspace group regardless of the origin choice, whereas when $|m| + |n| \geq 2$ are included the choice of noncentric origins yields polar structures.

Le Bail analysis of the higher Q-resolution room temperature synchrotron data for the ground-crystal sample allows some of the satellite reflections which overlap in the single crystal and SAED data to be resolved. (e.g., $11\bar{0}\bar{1}$ and $0001\bar{}$ both occur at $1/2\mathbf{a}^*+1/2\mathbf{b}^*$ within experimental error in the single crystal experiment); the components of the $\mathbf{p}^*$ and $\mathbf{q}^*$ vectors have been refined to the following values: $\alpha = 0.4925(2)$, $\beta = 0.4799(7)$ (Figure 2b), clearly demonstrating the incommensurate character of the modulations.

Analysis of the single crystal data is not possible in an incommensurate model due to the limitations in Q-resolution described above. However such approach can be undertaken with powder diffraction data. Further Rietveld refinement of the synchrotron powder XRD pattern was performed using the JANA2006 program.[37,39] While these yielded improved fits compared to the commensurate multiphase refinements originally employed, the oxygen−oxygen distances and Bi bond valence sums were in some cases unphysical, as domination of the X-ray scattering by bismuth renders the refinement relatively insensitive to the exact oxygen positions.

Table 2. Summary of Rietveld Refinement Parameters for Room Temperature D2b Data from $Bi_2Mn_{4/3}Ni_{2/3}O_6$

a (Å)	5.5729(1)
b (Å)	7.7686(2)
c (Å)	5.5091(2)
p^a	0.4930(3) 0 0
q^a	0 −0.4210(7) 0
χ^2	1.50
parameters (profile and background)	97(27)
R_{wp} (%)	3.09
$R_w(F)$ overall (%)[a]	2.06
main (%)	1.65
first order (%)	2.17
second order (%)	2.17

[a] $R_w(F)$ main refers only to peaks where $|n| + |m| = 0$, first-order peaks where $|n| + |m| = 1$ and second-order peaks where $|n| + |m| = 2$ and overall to all peaks.

Thus, in order to obtain a better analysis of the incommensurate structure, refinements were carried out against neutron powder diffraction data collected on the D2b diffractometer on a sample prepared via a ceramic route. Le Bail fits showed that all the peaks except those associated with the small $Bi_{12}MO_{20}$ impurity sillenite phase could be adequately fitted using a single incommensurate phase, with somewhat different modulation vectors from those found for the ground-crystal sample ($\alpha = 0.4930(3)$, $\beta = 0.4210(7)$). Here α is within 2 esd of the value obtained from ground single crystals and β has decreased from 0.4799(7).

Rietveld refinements were carried out using a 15 term Legendre polynomial for the background and a pseudo-Voigt peak shape. Bismuth positions were freely refined; however, the Mn/Ni−O distances were restrained to be in the range 2.0(±0.3) Å. It was also found that occupational modulation waves modeling the Mn/Ni distribution on the B site improved the fit ($\chi^2 = 1.50$ versus $\chi^2 = 1.93$) in the absence of occupational modulation. The neutron data are particularly sensitive to ordering on the B site due to the strong contrast between Mn and Ni given by the negative scattering length of Mn. Refined positional and occupational parameters are listed in Tables 2 and 3, respectively, the anisotropic thermal parameters are available in the Supporting Information, and the final refinement is shown in Figure 4. A structural approximant cell based on the minimal rational approximants is shown in Figure 5 ($\alpha \sim 35/71$, $\beta \sim 8/19$ to within experimental error). The enlarged regions reveal the Ni/Mn order, octahedral geometry, and tilting.

Before discussing what can be learned from the Rietveld refinement it should be born in mind that the use of a Fourier series with a small number of terms is not necessarily a good description of the modulation, particularly if the modulation represents two or more distinct atomic environments, or for a sharply varying displacement.[50,51] Some ordering of the nickel and manganese is apparent from Figure 5, supported by BVS calculations in Figure 6a,b; regions rich in Mn correspond to

(50) Evain, M.; Petricek, V. *Ferroelectrics* **2004**, *305*, 43–48.
(51) Petricek, V.; Vanderlee, A.; Evain, M. *Acta Crystallogr., Sect. A* **1995**, *51*, 529–535.

Table 3. Summary of the Refined Structural Parameter for 293 K Neutron Powder Diffraction Data from $Bi_2Mn_{4/3}Ni_{2/3}O_6$[a]

Positional Parameters

atom	modulation	*x*	*y*	*z*	U_{iso}
Bi		–0.0106(4)	1/4	0	0.0290(10)
	s,1,0	–	–	0.0271(7)	
	c,1,0	–	–	–0.0327(9)	
	s,0,1	–	–	0.0083(13)	
	s,1,1	0.0100(13)	–0.0036(6)	–	
	c,1,1	0.0035(9)	0.0013(7)	–	
	s,1,–1	–0.0100(13)	–0.0036(6)	–	
	c,1,–1	–0.0035(9)	0.0013(7)	–	
Mn		0	0	1/2	0.071(4)
	s,1,0	–	–	–0.030(2)	
	s,0,1	–	–	0.011(2)	
	s,1,1	–0.010(3)	0.0090(19)	–	
	s,1,–1	–0.005(3)	0.0042(19)	–	
O1		0.0705(6)	1/4	1/2	0.0281(16)
	s,1,0	–	–	–0.0459(12)	
	c,1,0	–	–	0.0442(12)	
	s,0,1	–	–	0.0240(16)	
	s,1,1	0.0059(11)	0.0102(8)	–	
	c,1,1	–0.0007(11)	–0.0023(8)	–	
	s,1,–1	–0.0059(11)	0.0102(8)	–	
	c,1,–1	0.0007(11)	–0.0023(8)	–	
O2		1/4	–0.0403(3)	1/4	0.0552(16)
	s,1,0	–0.0184(11)	–	–0.0435(9)	
	c,1,0	–	0.0134(7)	–	
	s,0,1	0.0198(13)	–	0.0197(13)	
	c,0,1	–0.0006(15)	–	0.0065(16)	
	s,1,1	–0.0055(11)	0.0013(6)	0.0008(12)	
	c,1,1	–0.0040(13)	0.0013(5)	–0.0089(12)	
	s,1,–1	0.0055(11)	0.0013(6)	–0.0008(12)	
	c,1,–1	–0.0040(13)	–0.0013(5)	–0.0089(12)	

Occupational Waves

atom	modulation	occupancy
Mn		0.667[b]
	c,1,1	0.142(13)
	c,1,–1	–0.054(15)

[a] Up to four modulation waves were considered for each parameter **p***, **q***, **p*** + **q*** and **p*** − **q***. Modulation terms are labelled by three characters: the first refers to whether it is a sine (s) or cosine (c) term, the first number refers to the *p* component and the second the *q* component. Only terms allowed by symmetry are listed. [b] Fixed during the refinement.

regions where the BVS for Mn on the B site approaches the expected value of 3.5 and similarly in regions of elevated Ni occupancy the BVS tends toward 2 for Ni on the B site. This cross-correlation of the refined occupancy with the refined modulated cation and anion positions further validates the observed partial B site ordering. The variations of the Bi−O and Mn/Ni−O bond lengths as a function of *u* and *t* are shown in Figure S2 and Figure 7 respectively.

The superspace group of $Bi_2Mn_{4/3}Ni_{2/3}O_6$ is centrosymmetric (*Ibmm(α00,0-β0)mm.ss*). Despite its global symmetry being centrosymmetric, the modulated nature of the $Bi_2Mn_{4/3}Ni_{2/3}O_6$ phase is compatible with the existence of polar regions within the structure.

In a truely incommensurate material, the structure cannot be produced from the 3D translation of an elementary cell. However, a representative sampling of the atomic positions can be obtained using a large enough approximant, allowing a relatively good approximation of the polarization to be determined. Alternatively, integrating the polarization over all values of *t* and *u* directly from the 5D result would give the overall polarization.

In the first approach, the polarization was calculated by constructing an approximant.[49] The atomic positions were then derived and the polarization calculated assuming ionic point charges, with charge or chemical ordering of the Mn or Ni omitted. An approximant of size $2\sqrt{2}a_p \times 4a_p \times \sqrt{2}a_p$ (using the best origin found in the single crystal refinements) yields a polarization of 56 μC/cm^2 along **a**, very similar to the value obtained for the original refinement of 60 μC/cm^2[33] in $P2_1mn$ and to 85 μC/cm^2 based on the commensurate modulated refinement of the single crystal data above. However if we consider the larger approximant of size $71\sqrt{2}a_p \times 38a_p \times \sqrt{2}a_p$ (Figure 5) we obtain a significantly reduced polarization of 2 μC/cm^2, suggesting that the modulation suppresses **P**.

The alternative method consists of the direct use of the super space results. A sampling of 32 unique origin points in the internal space ($t = n/16$, $u = n/16$; $t < 0.5$, $u < 0.5$ where n is an integer) was selected, atomic positions were calculated using JANA2006 within an approximant cell of the same size as the initially used commensurate cell, and the polarization was evaluated as in the first example above. Figure 8 provides the resulting global depiction of the polarization in the 5D supercrystal.[49] It shows the global nonpolar character of the structure because the vector sum of the calculated polarizations is zero, and allows also the identification of significant nonzero polarization over shorter length scales corresponding to the size of the $2\sqrt{2}a_p \times 4a_p \times \sqrt{2}a_p$ commensurate cell, because several of these approximants do have a net polarization, as represented

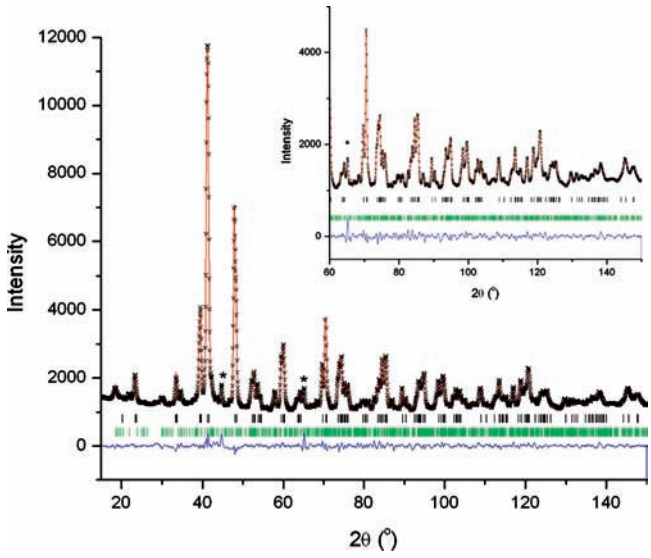

Figure 4. Final 5-D incommensurate Rietveld refinement of room temperature neutron powder diffraction (D2b $\lambda = 1.59452(3)$ Å) data from $Bi_2Mn_{4/3}Ni_{2/3}O_6$ (a) full scale (b) magnified view showing high angle region. Black tick marks represent substructure peaks (*hklmn*; *m*,*n* = 0) and green tick marks represent peaks where at least one of *m*,*n* ≠ 0 (* denotes $MnBi_{12}O_{20}$ type impurity).

by the arrows. The distance over which the polarization is suppressed is larger than the size of the commensurate cell but smaller than the large approximant cell, setting bounds on the size of these local polar regions.

The long period polarization-suppressing modulation of the basic ferroelectric unit (as defined by the original small polar commensurate cell) is consistent with a null response from a powder second harmonic generation (SHG) measurement.[43,52] Given the physical measurements reported above and the quality of the fit, no attempts were made to fit the data using other representations of the modulation or based on a polar subcell. The structure is strongly distorted around Bi (See Figure S2 and Figure 9). Visualization of how this polar local environment is canceled by the incommensurate modulation in real space is not easy due to the complex nature of the displacements. This can be simplified somewhat by considering only the displacements of the bismuth atoms from the centroids of the BiO_{12} cages. Figure 10 represents these displacements for two cases: a short-range $2\sqrt{2}a_p \times 4a_p \times \sqrt{2}a_p$ approximant equivalent to the previously reported single crystal structures,[33] which shows the complex nature of the bismuth displacements even in the small approximant cell, and a longer range approximant $2\sqrt{2}a_p \times 38a_p \times \sqrt{2}a_p$; the two insets show an approximate mirror relationship between two locally polar regions which leads to the cancellation of the polarization apparent from the small commensurate cell used originally.

High-Temperature Structure. Though the material has significant electronic conductivity at high temperature ($\sim 10^{-4}$ S cm^{-1} at ambient temperature, which is significantly higher than for $BiFeO_3$.[53]), measurements of the relative permittivity (ε_r) and loss tangent tan(δ) clearly show an anomaly between 150 and 200 °C (Figure S3) indicative of a phase transition. Selected area electron diffraction patterns above and below this transition were measured (Figure S4). The high temperature phase has been studied at 300 °C. The phase transition has been observed at lower temperature (around 200 °C) during the heating ramp, but we chose this temperature to avoid an incomplete transition. The most significant change in the electron diffraction patterns (Figure 3) is the disappearance of the modulation as more intense and weak reflections no longer coexist. The reconstruction of the reciprocal space at this temperature exhibits an $a = \sqrt{2}a_p$, $b = \sqrt{2}a_p$, and $c = 2a_p$ cell with the following extra conditions: $0kl{:}k + l = 2n$; $h0l{:}h = 2n$ (*hkl*: no general condition). Two different space groups are then possible: *Pnam* and $Pna2_1$. To better follow the evolutions during the phase transition, we kept the same setting that used in the ambient temperature study (same axis labeling). The *Pnam* space group obtained corresponds in fact to the more common non polar *Pnma* by an $a\bar{c}b$ permutation.

The [100] HREM image (Figure S4(d)) of the high temperature phase is clearly different from the corresponding image (Figure 1) at ambient temperature. The $4a_p$ and $2\sqrt{2}a_p$ cell parameters can indeed no longer be observed and are respectively replaced by $2a_p$ and $\sqrt{2}a_p$ cell parameters. A centering condition appears on this plane, proving a structural rearrangement.

Variable-temperature neutron diffraction data were collected on GEM at ISIS to refine the high-temperature structure. (Figure S5 and Tables S1 and S2). As can be seen in Figure 11, the peaks associated with the modulation decrease in intensity dramatically with increasing temperature, and the subcell (111) reflection grows in intensity. On cooling, hysteresis is observed in the intensity of the (111) reflection, due either to a first-order transition between the low temperature modulated structure and the high temperature commensurate phase, or to strain. Careful examination of the higher quality data set used for the Rietveld refinement shows that the more intense modulation peaks from the low-temperature structure, though now much less intense and broader, are still present. The persistence of some superstructure peaks, though broadened, may be due to the persistence of short-range order of the displacements above the transition as observed in mellilite systems such as $Ca_{0.84}Sr_{0.16}MgSi_2O_7$[54] or may be due to the persistence of some Mn/Ni order on the B site. The latter explanation is consistent with the partial metal ordering on the octahedral sites refined in the low temperature phase, as the transition metals are unlikely to diffuse at such low temperatures. The contrast due to this short-range order of Mn and Ni would be strongest in neutron diffraction, in comparison with XRD or ED.

Two main changes are noticeable in the bond lengths. Above the transition, the Mn/Ni−O_6 octahedra are very regular with the three crystallographically distinct Mn/Ni−O distances varying by only 0.003 Å, whereas they are significantly different below the transition (Figure 7), though the exact details of the distortion are somewhat obscured by the small number of sine and cosine terms used. In addition the local Bi coordination environment above the transition is still polar but now ordered in a simple antiferroelectric fashion as can be seen from the structure (Figure S5) i.e. the modulation in the low-temperature structure corresponds to the suppression of the local polarization around Bi^{3+}, which arises from the lone-pair-driven displacement from the centroid of the coordinating oxygen polyhedron, over a longer distance than in the simple commensurate antiferroelectric high-temperature structure.

(52) Halasyamani, P. S.; Poeppelmeier, K. R. *Chem. Mater.* **1998**, *10*, 2753–2769.
(53) Jhih-Cyun, C.; Jenn-Ming, W. *Appl. Phys. Lett.* **2007**, *91*, 182903.
(54) Kusz, J.; Bohm, H. *Z. Kristallogr.* **2001**, *216*, 509–512.

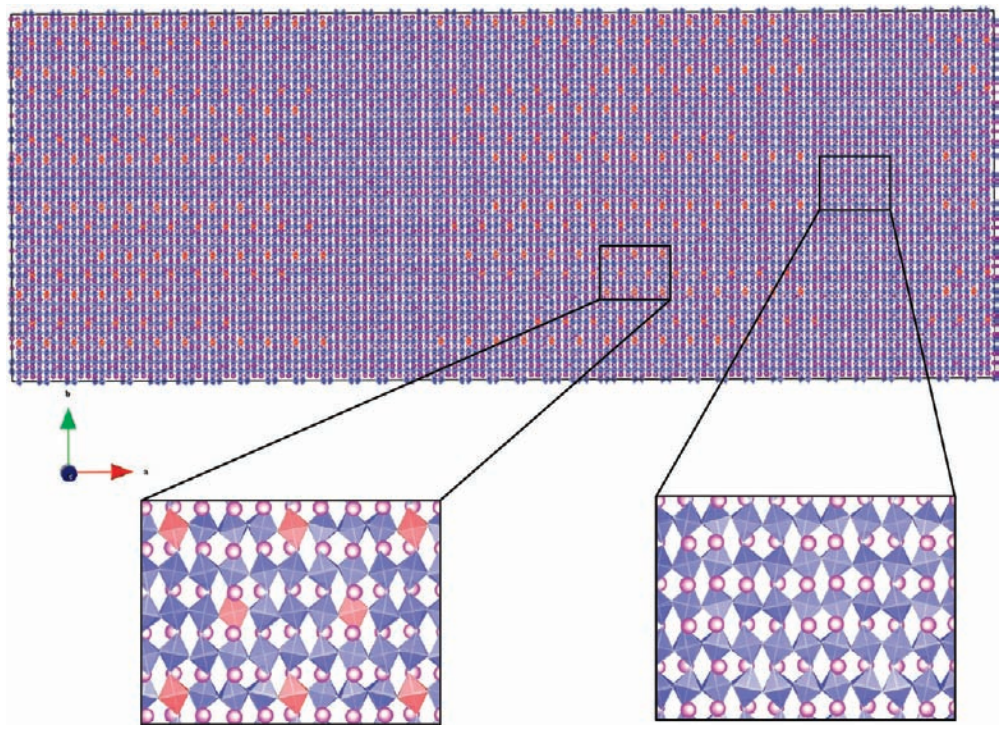

Figure 5. Approximant cell ($71\sqrt{2}a_p \times 38a_p \times \sqrt{2}a_p$) for $Bi_2Mn_{4/3}Ni_{2/3}O_6$ at room temperature, drawn from the incommensurate refinement viewed down the nonmodulated c axis. Blue octahedra have >50% Mn occupancy and red octahedra >50% Ni. This approximant cell is of a sufficient size to provide a view of the range of environments and represents the commensurate cell that is within the experimental error on the modulation vectors for $Bi_2Mn_{4/3}Ni_{2/3}O_6$.[38] The expanded regions show the B cation site order and the acceptable geometry and the tilting of the octahedra.

Magnetism and Magnetoelectric Coupling. Magnetic susceptibility measurements recorded in low field indicate a divergence between the zero-field-cooled (ZFC) and field-cooled (FC) magnetization below 37.0(5) K (Figure S6), which was taken as the magnetic freezing temperature of the sample (T_{sg}). Between 200 and 300 K the data were fitted by the simple Curie−Weiss law (θ = 84.1(4) K; C = 4.94(1) emu K/mol). These values are considerably higher than the expected values of C = 3.92 emu/mol and μ_{eff} = 5.60 μ_B/mol which are based on $Mn^{4+}/Mn^{3+}/Ni^{2+}$ in the ratio 33%, 33%, 33%, suggested by the composition. However, analysis of XAS data (Figure S7) shows that the material has a Ni valence of approximately 2 and a Mn valence higher than 3, given the shift relative to $BiMnO_3$, confirming the valence states expected on the basis of charge balancing the initial composition. This indicates that the higher than expected Curie constants are probably an artifact of the limited temperature range used (the maximum measurement T is only 3 × θ_W), and the strong but frustrated magnetic exchange coupling.

Variable-temperature neutron diffraction data recorded on D2b at the ILL above and below the transition revealed no extra scattering (Figure S8). The lack of magnetic Bragg diffraction is consistent with the transition not being to a magnetically ordered state but rather to a spin-glass-like state, confirmed by the displaced hysteresis loop apparent in the FC dc $M(H)$ isotherm and the weak frequency dependence of the ac susceptibility from the crystal sample (Figure 12). The magnetic susceptibility of a spin glass has a nonlinear contribution that diverges at T_{sg}, which implies a strong magnetic field dependence of the magnetic susceptibility is expected, such that the application of a small magnetic field can cause the system to behave like a ferromagnet. The high-field $M(H)$ data do not saturate[33] but approach a value of 3.54 μ_B per formula unit, which is considerably less than the 6 μ_B per site expected for fully ferromagnetic coupling. $M(H)$ loops were collected as a function of temperature for a ceramic sample (Figure S9) and show that the remanent magnetization decreases rapidly with temperature and has disappeared by 30 K, although the $M(H)$ curve is still significantly nonlinear, well above the transition.

Muon spin resonance data were collected on $Bi_2Mn_{4/3}Ni_{2/3}O_6$ as a function of temperature. At high temperature (300 K) we observe spin relaxation which follows simple exponential behavior. (Figure 13) This is the typical behavior of a paramagnet, where dynamic spin fluctuations relax the muon spins. This leads to a relaxation rate λ proportional to $\delta^2\nu^2$, where λ is the width of the magnetic field distribution probed by the muons and ν is the field fluctuation rate. As the temperature is lowered from ∼300 K, we observed an increase in the relaxation rate, which corresponds to a decrease in the fluctuation rate of the local magnetic field as the paramagnetic spin fluctuations slow upon cooling. Below ∼40 K, the initial asymmetry falls sharply, and the relaxation rate decreases. This can be explained by the freezing of the spins on the muon time scale, leading to an internal field at the muon site which causes muon precession faster than $1/t_{pulse}$, where $t_{pulse} \sim 70$ ns and hence not directly observable at ISIS. The temperature dependence of the initial muon polarization thus shows a transition from a frozen phase to a paramagnetic phase at 37 K.

The variation in the cell parameters and modulation vectors with temperature in 1 K intervals between 40 and 25 K was evaluated by profile matching of neutron diffraction data from GEM with FullProf.[55] The data were fitted with five separate phases, one being the subcell in the space group *Ibmm*, and four phases containing each combination of the modulation vectors used to describe the incommensurate structure, $\mathbf{p}^*$, $\mathbf{q}^*$, $\mathbf{p}^* + \mathbf{q}^*$, and $\mathbf{p}^* - \mathbf{q}^*$. The subcell parameters and absolute

(55) Rodriguez-Carvajal, J. *Physica B* **1993**, *192*, 55–69.

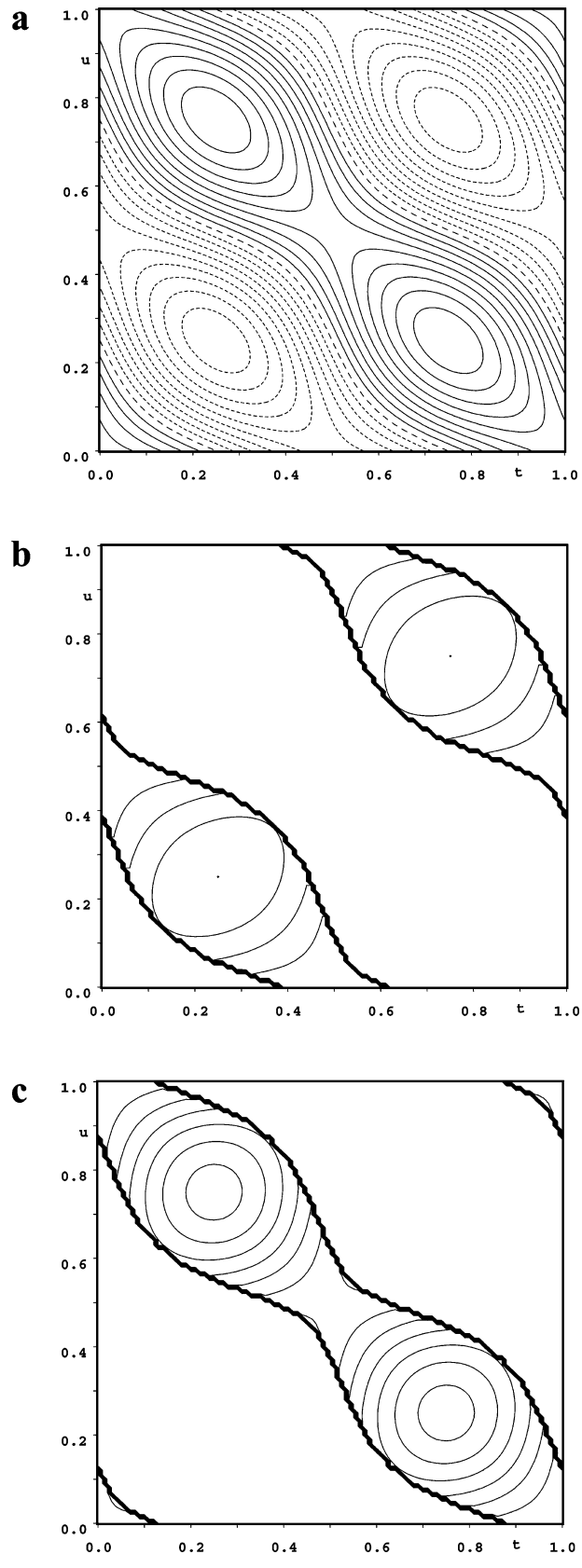

Figure 6. Variation of (a) Mn occupancy (solid contours >0.667 dashed <0.667, contours are in 0.02 increments) (b) Ni BVS for regions with Ni occupancy >0.4 (contours are in 0.1 increments, minimum of 2.04 at ~1/4,1/4), (c) Mn BVS for regions with Mn occupancy >0.73 (contours are in 0.1 increments, maximum of 3.54 at ~1/4,3/4).

values of the modulation vectors were constrained to be the same in each phase. The fits showed a clear change in trend in the subcell parameters (35(1) K) (Figure 14) in the region of the magnetic transition temperature. The variation of α and β is not reported due the inability to limit the values of m and n, as both are close to half in profile fitting, and this tends to prejudice the values toward 1/2 as the higher-order satellites tend to the positions of the subcell Bragg peaks. The subcell parameter anomalies show the coupling between the lattice and the magnetic d-electrons from the ions occupying the octahedral sites. The effect is particularly marked in the *a* subcell parameter whose first temperature derivative changes sign at the magnetic transition; this is consistent with the local polarizations apparent in the incommensurate structure analysis lying within the *ab* plane.

The temperature dependence of the relative permittivity has been measured at 0 T and at 13 T in the region of the spin-glass transition, where the loss tangent is smaller than 10^{-3} and the relative permittivity has a value of 68. There is a small anomaly in the relative permittivity at the spin-glass transition that is visible in the derivative data (Figure 15a), showing a coupling between dielectric response and magnetic ordering. This anomaly disappears under the application of a 13 T field. The existence of an anomaly at the temperature of the magnetic transition has also been revealed in several magnetic insulators such as $Co_3V_2O_8$,[56] $Ca_3Co_2O_6$,[57] or $BiMnO_3$[22] and in polar antiferromagnets such as $YMnO_3$,[58] showing a coupling between dielectric and magnetic properties.

The magnetic field dependence of the relative permittivity has been studied in order to clarify this coupling (Figure 15b). Two competing temperature-dependent behaviors have been revealed: one far below the spin-glass transition (5 K) similar although opposite in sign to that observed for $BiMnO_3$[22] near T_c and another quadratic field response appearing when increasing the temperature. This competition gives an original shape to the permittivity-field relationship near the spin-glass transition. The order parameter of a spin-glass transition is the nonlinear magnetic susceptibility, and its coupling with the local polarization has not been resolved theoretically.

Discussion

The original conventional supercell and the current commensurate modulated superstructure ($\alpha, \beta = 1/2$) approaches both suggest that a substantial polarization develops in $Bi_2Mn_{4/3}Ni_{2/3}O_6$ below 423 K. Although there is a maximum in the relative permittivity at this temperature, NLO measurements give no indication of the absence of a center of symmetry. The crystallographic and physical measurements are thus inconsistent when only a commensurate modulation is considered, as the investigation of all space groups consistent with the diffraction data clearly indicate that the commensurate unit cell is polar. The explanation for this requires that the slightly incommensurate nature of the modulation is taken into account in order to obtain an understanding of how the polarization which clearly emerges from both commensurate refinements is lost. This is challenging as only a small number of reflections arising from the modulation are observed, and only powder data are available with sufficient Q resolution to detect the incommensurability

(56) Bellido, N.; Martin, C.; Simon, C.; Maignan, A. *J. Phys.: Condens. Matter* **2007**, *19*, 7.
(57) Bellido, N.; Simon, C.; Maignan, A. *Phys. Rev. B* **2008**, *77*, 4.
(58) Huang, Z. J.; Cao, Y.; Sun, Y. Y.; Xue, Y. Y.; Chu, C. W. *Phys. Rev. B* **1997**, *56*, 2623–2626.

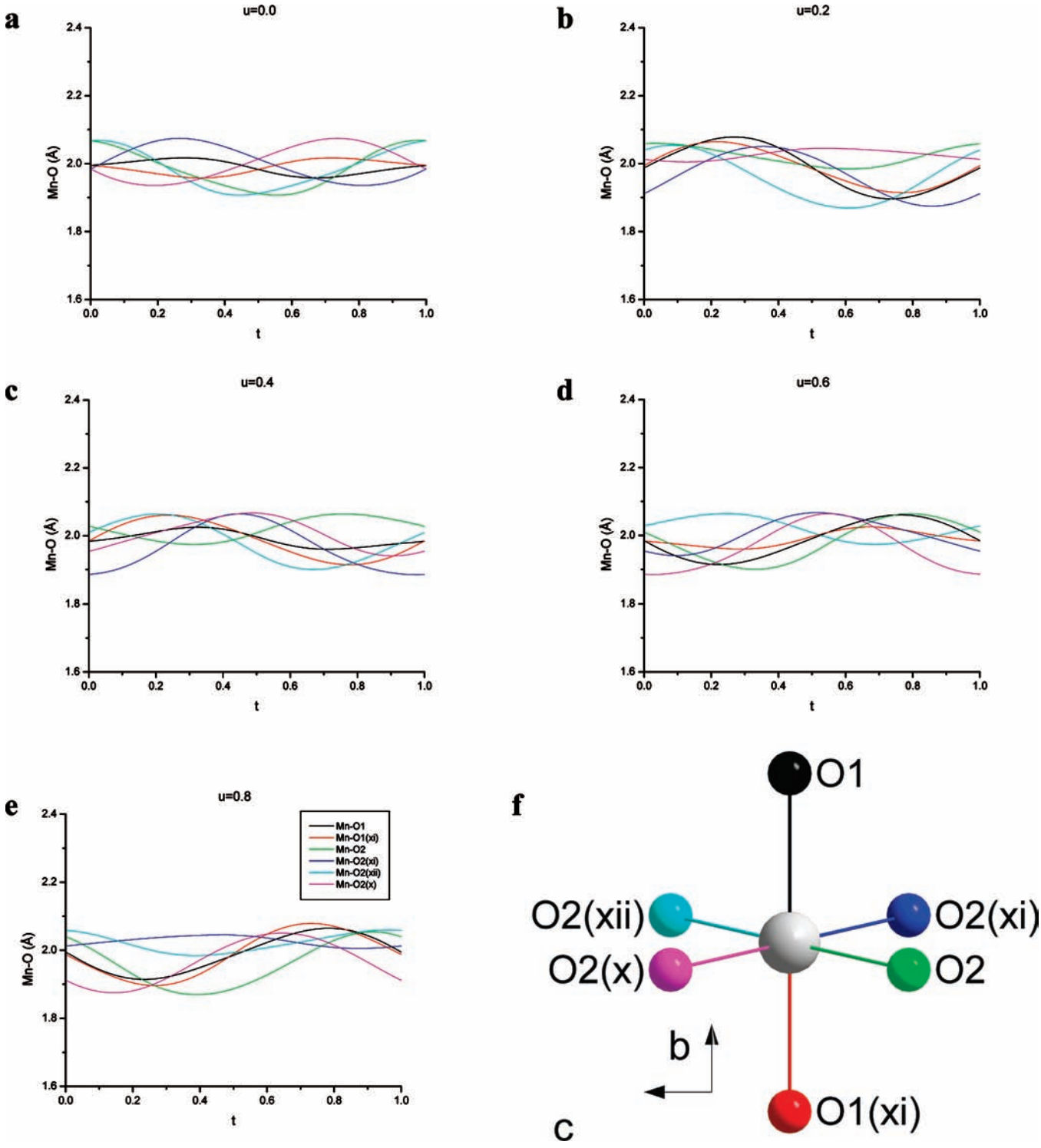

Figure 7. Variation of Mn/Ni−O distances as a function of t at (a) $u = 0$, (b) $u = 0.2$, (c) $u = 0.4$, (d) $u = 0.6$, (e) $u = 0.8$. The MnO_6 octahedron from the subcell is shown in (f) where the Mn atom is gray and the O atoms are color coded to match the plots. Symmetry labels are the same as those used in Table 4.

of the modulation (Figure 2). Given the physical properties observed, the incommensurate modulation can be treated in terms of sine and cosine terms as these in the truly incommensurate case will always yield centric structures as the modulation of a nonpolar subcell possesses a center of symmetry. Analysis of the approximant produced from the incommensurate modulation reveals a considerably reduced polarization, as expected, and indicates that the structure is locally polar (i.e., shows the existence of acentric domains within the centric structure) (Figure 8). The incommensurate character of the modulation is indeed compatible with the existence of acentric domains where a nonzero polarization occurs, but this polarization is reduced to zero over a large enough length scale. (Figure 9 shows how the Bi displacements within the large approximant cell are centrosymmetrically disposed around the subcell Bi positions).

Incommensurate modulations in stoichiometric perovskites are found in three main groups of compounds, lead perovskites such as Pb_2CoWO_6,[59,60] Pb_2MgTeO_6,[61,62] Pb_2CdWO_6,[63]

Table 4. Summary of the Interatomic Distances for the Refined Structure of $Bi_2Mn_{4/3}Ni_{2/3}O_6$[a]

bond	average (Å)	min (Å)	max (Å)
Bi−O1(i)	2.789(15)	2.217(18)	3.366(12)
Bi−O1	2.822(15)	2.217(18)	3.366(12)
Bi−O1(iv)	3.14(4)	2.85(5)	3.49(5)
Bi−O1(v)	2.47(4)	2.03(5)	2.78(5)
Bi−O2	3.05(3)	2.56(3)	3.62(3)
Bi−O2(vi)	2.52(3)	2.00(4)	3.12(3)
Bi−O2(vii)	2.53(3)	2.01(4)	3.12(3)
Bi−O2(v)	3.03(3)	2.56(3)	3.62(3)
Bi−O2(iii)	2.53(3)	2.00(4)	3.12(3)
Bi−O2(viii)	3.05(3)	2.56(3)	3.62(3)
Bi−O2(ix)	3.05(3)	2.56(3)	3.62(3)
Bi−O2(x)	2.55(3)	2.01(4)	3.12(3)
Mn−O1	1.99(3)	1.88(3)	2.16(2)
Mn−O1(xi)	1.99(3)	1.88(3)	2.16(2)
Mn−O2	2.00(3)	1.80(3)	2.13(3)
Mn−O2(xi)	2.00(3)	1.80(3)	2.13(3)
Mn−O2(xii)	2.00(3)	1.80(3)	2.13(3)
Mn−O2(x)	2.00(3)	1.80(3)	2.13(3)
O1−O1(v)	3.44(2)	2.86(4)	3.96(3)
O1−O1(xiii)	3.40(3)	2.86(4)	3.96(3)
O1−O2	2.86(3)	2.60(3)	3.06(3)
O1−O2(xiv)	2.78(3)	2.47(3)	3.06(3)
O1−O2(xi)	2.78(3)	2.47(3)	3.06(3)
O1−O2(v)	2.86(3)	2.60(3)	3.06(3)
O1−O2(iii)	2.78(3)	2.47(3)	3.06(3)
O1−O2(xii)	2.85(3)	2.60(3)	3.06(3)
O1−O2(xv)	2.86(3)	2.60(3)	3.06(3)
O1−O2(x)	2.78(3)	2.47(3)	3.06(3)
O2−O2(xvi)	3.24(3)	2.85(4)	3.49(4)
O2−O2(viii)	2.77(3)	2.28(3)	3.26(3)
O2−O2(xii)	2.76(3)	2.28(3)	3.26(3)
O2−O2(x)	2.88(4)	2.39(4)	3.14(3)
O2−O2(vii)	2.89(4)	2.39(4)	3.14(3)

[a] (i) x, y, $-1+z$; (ii) $-x$, $1/2+y$, $-1+z$; (iii) $-x$, $1/2+y$, z; (iv) $-1/2-x$, $1/2-y$, $1/2-z$; (v) $1/2-x$, $1/2-y$, $1/2-z$; (vi) $-1/2+x$, $1/2+y$, $-1/2+z$; (vii) $-x$, $-y$, $-z$; (viii) $1/2-x$, $1+y$, $-1/2+z$; (ix) x, $1/2-y$, $-z$; (x) $-1/2+x$, $1-y$, $1/2-z$; (xi) $-x$, $-y$, $1-z$; (xii) $1/2-x$, $1+y$, $1/2+z$; (xiii) $1/2-x$, $1/2-y$, $3/2-z$; (xiv) $-1/2+x$, $1/2+y$, $1/2+z$; (xv) x, $1/2-y$, $1-z$; (xvi) $1/2-x$, $-1/2-y$, $1/2-z$; (xvii) $1/2+x$, $1-y$, $1/2-z$.

$PbSc_{1/2}Ta_{1/2}O_3$,[64] organic inorganic perovskites,[65−67] and charge-ordered/orbital-ordered systems, where the manganites are particularly heavily studied, e.g. $La_{1/2}Ca_{1/2}MnO_3$[68] and recently in $Bi_{1-x}Sr_xMnO_3$[69] although these generally are only incommensurate in a limited temperature range near the charge-ordering transition, though no manganites have been fully refined in the incommensurate phase. The origin of the incommensurate modulations observed in the lead systems is unclear,[70,71] although the active lone pair appears to be important, and as in the current case, it is the A site that displays the most heavily modulated bond length variation.[59] Given that the octahedral distortions at the B site disappear above the incommensurate−commensurate transition (though still permitted by symmetry for the $GdFeO_3$ structure) and the conductivity data show a distinct kink (Figure S10), it is likely that some degree of charge and/or orbital order is also present in $Bi_2Mn_{4/3}Ni_{2/3}O_6$, given the similar behavior observed in $Bi_{1-x}Sr_xMnO_3$.[69] This material thus presents coupling of the displacements centered around Bi and those associated with electronic ordering at the B site.

At high temperatures $Bi_2Mn_{4/3}Ni_{2/3}O_6$ adopts the $GdFeO_3$ structure which is an antiferroelectrically distorted perovskite with the Bi sites displaced along **a** in the setting used, as can be seen in Figure S5. This is also the largest component of most of the displacements in the incommensurate phase; indeed, the $GdFeO_3$ structure is obtained if $\alpha, \beta = 1$ for the superspace group *Ibmm(α00,0-β0)mm.ss* of the incommensurate structure. In general, incommensurate modulations result from the competition of different interactions. One potential explanation of the modulation would therefore be an incommensurate charge ordering/orbital ordering on the partially cation-ordered B sites where the Mn site has a mean valence of +3.5 which is known to particularly strongly favor charge ordering, strongly coupled to A site Bi displacements via the BO_6 octahedral distortions to generate a locally polar coupling of the individual A site environments. Indeed it is well-known that Bi-containing manganites show unusually high charge ordering temperatures.[45,46,69] Both $Bi_{3/4}Sr_{1/4}MnO_3$[45] and $Bi_{2/3}Sr_{1/3}MnO_3$[46] show similar although commensurate modulations of an *Ibmm* subcell: the former adopts an *Ibmm* structure above the charge ordering transition (∼575 K), while the later adopts a Pbmn ($GdFeO_3$) structure (∼550 K). Recent studies on single crystals have shown similar behavior with a narrow range of incommensurability.[69] Similar behavior is observed in the $Bi_{1-x}Ca_xMnO_3$[72,73] system though the ordering temperatures are lower and a single modulation. The bismuth sites are more distorted (Figure S2 and Table 3) than those in $BiFeO_3$ (3 × 2.267(1) Å 3 × 2.534(1) Å 3 × 3.208(2) Å and 3 × 3.447(2) Å)[74] partly due to the displacements being primarily along $[110]_p$ rather than $[111]_p$ i.e. toward bridging oxygens rather than the octahedral faces. The spread in the observed B−O distances (Figure 7, Table 3) is similar to that found in Jahn−Teller orbitally ordered phases such as $PrMnO_3$[75] (Mn−O 2 × 1.9530(5), 2 × 1.909(2) and 2 × 2.210(2) Å) and charge ordered manganites such as $Bi_{0.6}Ca_{0.4}MnO_3$[73] (Mn(1)−O 2.08(2), 2.07(1), 1.90(1) 1.91(1) 1.94(1) and 1.95(1) Å and Mn(2)−O 2 × 1.95(3), 2 × 1.96(1), 1.88(1) Å) and 2.07(1) Å), $Pr_{1/2}Ca_{1/2}MnO_3$[76] and

(59) Baldinozzi, G.; Calvarin, G.; Sciau, P.; Grebille, D.; Suard, E. *Acta Crystallogr., Sect. B* **2000**, *56*, 570–576.
(60) Bonin, M.; Paciorek, W.; Schenk, K. J.; Chapuis, G. *Acta Crystallogr., Sect. B* **1995**, *51*, 48–54.
(61) Baldinozzi, G.; Grebille, D.; Sciau, P.; Kiat, J. M.; Moret, J.; Berar, J. F. *J. Phys.: Condens. Matter* **1998**, *10*, 6461–6472.
(62) Baldinozzi, G.; Sciau, P.; Moret, J.; Buffat, P. A. *Solid State Commun.* **1994**, *89*, 441–5.
(63) Sciau, P.; Grebille, D. In *Aperiodic 94, Proceedings of the International Conference on Aperiodic Crystals*; Chapuis, G., Paciorek, W., Eds.; World Scientific: Singapore, 1995; pp 460−464.
(64) Randall, C. A.; Markgraf, S. A.; Bhalla, A. S.; Baba-Kishi, K. *Phys. Rev. B* **1989**, *40*, 413–16.
(65) Swainson, I. P. *Acta Crystallogr., Sect. B* **2005**, *B61*, 616–626.
(66) Fuetterer, K.; Depmeier, W.; Petricek, V. *Acta Crystallogr., Sect. B* **1995**, *B51*, 768–79.
(67) Fuetterer, K.; Withers, R. L.; Welberry, T. R.; Depmeier, W. *J. Phys.: Condens. Matter* **1995**, *7*, 4983–98.
(68) Chen, C. H.; Cheong, S. W. *Phys. Rev. Lett.* **1996**, *76*, 4042–4045.
(69) Yamada, S.; Matsunaga, T.; Sugano, E.; Sagayama, H.; Konno, S.; Nishiyama, S.; Watanabe, Y.; Arima, T.-H. *Phys. Rev. B* **2007**, *75*, 214431/1–214431/7.
(70) Caracas, R.; Gonze, X. *Phys. Rev. B* **2005**, *71*, xxxx.
(71) Kornev, I. A.; Bellaiche, L. *Phys. Rev. Lett.* **2002**, *89*, 115502/1–115502/4.
(72) Garcia-Munoz, J. L.; Frontera, C.; Beran, P.; Bellido, N.; Lord, J. S.; Ritter, C.; Margiolaki, I. *J. Phys.: Condens. Matter* **2007**, *19*, 9.
(73) Giot, M.; Beran, P.; Perez, O.; Malo, S.; Hervieu, M.; Raveau, B.; Nevriva, M.; Knizek, K.; Roussel, P. *Chem. Mater.* **2006**, *18*, 3225–3236.
(74) Palewicz, A.; Przenioslo, R.; Sosnowska, I.; Hewat, A. W. *Acta Crystallogr., Sect. B* **2007**, *63*, 537–544.
(75) Sanchez, D.; Alonso, J. A.; Martinez-Lope, M. J. *J. Chem. Soc., Dalton Trans.* **2002**, 4422–4425.
(76) Daoud-Aladine, A.; Rodriguez-Carvajal, J.; Pinsard-Gaudart, L.; Fernandez-Diaz, M. T.; Revcolevschi, A. In *International Conference on Neutron Scattering*; Springer-Verlag: Munich, Germany, 2001; pp S1758−S1760.

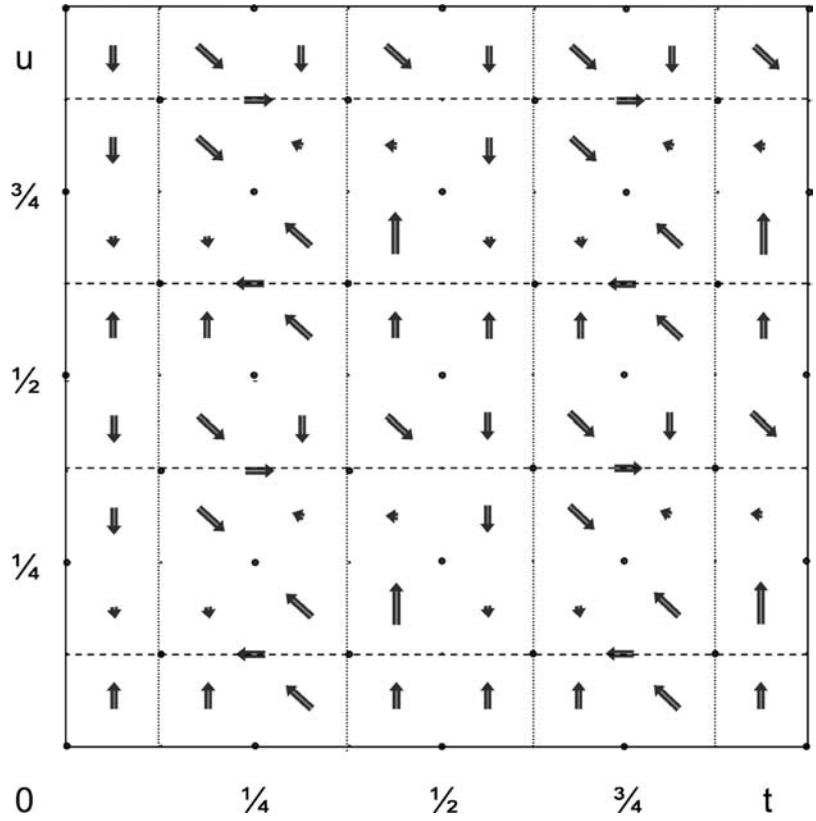

Figure 8. Schematic (*t*,*u*) representation of the cancellation of polarization within $Bi_2Mn_{4/3}Ni_{2/3}O_6$ in the internal space. Small circles represent null or weak polarizations (<0.1 μC/cm^2), arrows represent polar approximant cells of dimensions $2\sqrt{2}a_p \times 4a_p$, $\times \sqrt{2}a_p$ corresponding to polar regions within the crystal: resultants pointing along *t* represent polarizations parallel to **a** and along *u* polarizations parallel to **b**; the lengths are proportional to the magnitudes of the polarization. The two expanded regions in Figure 10 show how local regions of opposite **P**, corresponding to oppositely directed arrows in this figure, arise within the modulated structure.

$Bi_{3/4}Sr_{1/4}MnO_3$[77] For the mixed valence cases the degree of charge ordering as evidenced by BVS calculations is generally small,[77,78] and thus it is unsurprising that it cannot be detected in Figure 6. In each of the quoted cases the charge ordering is associated with a modulation of 1/2**a*** very similar to that observed for **p*** in $Bi_2Mn_{4/3}Ni_{2/3}O_6$. Indeed for the $Ln_{1-x}Ae_xMnO_3$ (Ln = Lanthanide, Ae = Alkali Earth) systems when $Mn^{III}/Mn^{IV} > 1$ this charge ordering modulation always take the value of 1/2 irrespective of the ratio,[79] though in the $Bi_{1-x}Ca_xMnO_3$[47] systems the modulation direction is a function of Mn^{III}/Mn^{IV}. Given also that the largest components of the modulation of the O positions are associated with the first modulation vector **p*** ($\sim$1/2**a***) it is likely that charge ordering plays a role in this modulation. It should also be noted that **p*** does not vary significantly between the ceramic and single crystal sample in line with the reported lack of variation observed for $Ln_{1-x}Ae_xMnO_3$ systems. However, it is not the factor affecting this modulation as it is also associated with the largest components of the bismuth displacements. In $Bi_2Mn_{4/3}Ni_{2/3}O_6$, the lone pair Bi^{3+} cation is undiluted on the A site, and so the polar local A site environment is a more pronounced feature of the resulting structure than in the diluted A site examples above. The competition between O displacements associated with the charge and orbital ordering reflected in the B−O distances and the O displacements associated the A environment relaxation together with those associated with chemical order on the B site generate a structure where complex bismuth displacements yield a long-period antiferroelectric phase but which locally appears polar on length scales shorter than the modulation, of the order of the polar commensurate cell edges ($\approx$20 Å) used originally.

These structural considerations at both high temperature (corresponding to the synthesis conditions) and ambient temperatures are of key relevance to the ambient pressure chemical stability of $Bi_2Mn_{4/3}Ni_{2/3}O_6$. At high temperature, the oxygen displacements required to allow the Bi cation to occupy the A site with the observed chemically sensible bond valence sum of +2.7 are accommodated by the partially ordered distribution of B site cations. At the synthesis temperatures the B site is charge-disordered, and therefore there are two distinct B cations (valence-disordered Mn and Ni): Bi is the only "asymmetric" ion, and the bond-length flexibility afforded by the presence of two distinct B site cations allows the perovskite material to form more readily than in a single B site case, with a small unit cell and antiferrolectric coupling of the lone-pair-driven polar BiO_{12} units. At the onset of the electronic ordering on the B site, the changes in the B−O bond lengths forces the Bi on the A site to coexist with not two but three (ordered Mn^{3+} and Mn^{4+}) species on the B site, requiring a more complex arrangement of Bi displacements. The coupling between BiO_{12} environments is now locally polar and only antiferroelectric over a longer distance. This would explain why the other two "multiple B site cation"[35] pure Bi A site perovskites have a much simpler ambient T structure because there is no need to accommodate

(77) Goff, R. J.; Attfield, J. P. *J. Solid State Chem.* **2006**, *179*, 1369–1374.
(78) Attfield, J. P. *Solid State Sci.* **2006**, *8*, 861–867.
(79) Van Tendeloo, G.; Lebedev, O. I.; Hervieu, M.; Raveau, B. *Rep. Prog. Phys.* **2004**, *67*, 1315–1365.

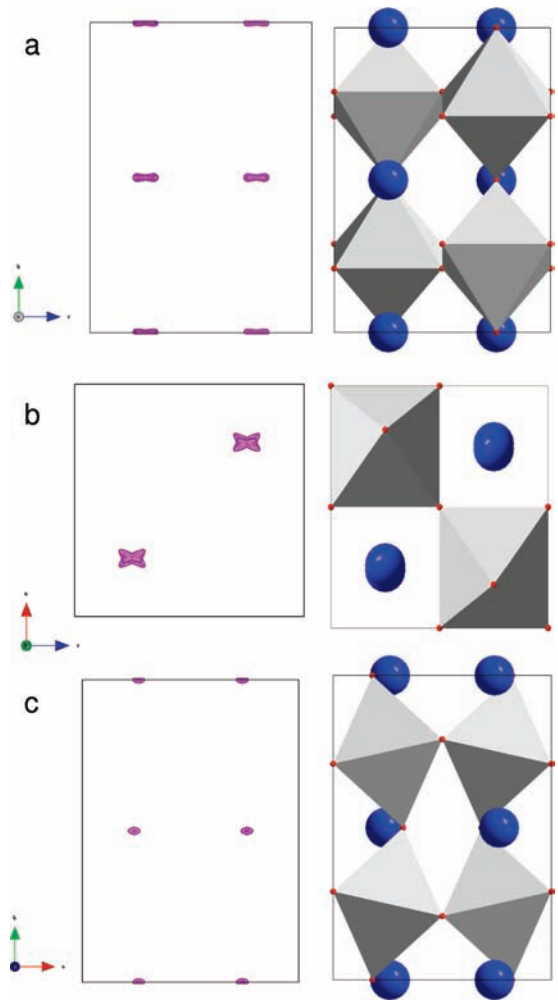

Figure 9. Displacements of the bismuth atoms in $Bi_2Mn_{4/3}Ni_{2/3}O_6$ within the approximant supercell of Figure 5 projected onto the subcell (left). The average structure is shown on the right. Viewing directions are (a) **a**, (b) **b** and (c) **c**.

electronic ordering at the B site. It is the competition between the polar A site displacements and the electronic-ordering induced B−O displacements on the partially cation ordered octahedral sites that produces the incommensurate modulation of $Bi_2Mn_{4/3}Ni_{2/3}O_6$. The partial cation order and distribution of B site valences also accounts for the frustration of magnetic long-range order.

The coupling of the incommensurate modulation with electronic ordering at the B site and polar displacements at the A site are of relevance to the high-pressure phase $BiMnO_3$ whose structure and dielectric properties have been the subject of considerable controversy.[18−21,23−25,80−83] Indeed, while Rietveld refinements show $BiMnO_3$ to be centric,[25,81,84] local probes appear to indicate that the material is noncentric.[23,24] Given that the reported physical properties of $BiMnO_3$ are often contradictory, it is worth exploring the conclusion of the current experiments that small deviations from commensurability can suppress polarization.[25,80,85−87] The cells of both structures are related to the *Ibmm* subcell, by a commensurate $\mathbf{p^*} = 1/2(\mathbf{a^*}+\mathbf{b^*})$ and $\mathbf{q^*} = 1/2(\mathbf{a^*}-\mathbf{b^*})$ modulation for $BiMnO_3$ and an incommensurate $\mathbf{p^*} = \sim 1/2\mathbf{a^*}$ and $\mathbf{q^*} = \sim -1/2\mathbf{b^*}$ modulation for $Bi_2Mn_{4/3}Ni_{2/3}O_6$. The possibility of a very small and as yet undetected deviation from commensurability producing the apparent polarity of the local structure of $BiMnO_3$ within an overall nonpolar/antiferroelectric material should be considered, by analogy with the apparent short-range polarity observed in $Bi_2Mn_{4/3}Ni_{2/3}O_6$ within the super-space description, in addition to the complexities introduced by the apparent nonstoichiometry of $BiMnO_3$.[26,27]

Another area worth investigating would be attempts to perturb the modulation of $Bi_2Mn_{4/3}Ni_{2/3}O_6$ either by growing thin films (films thinner than the modulations characteristic length may be inherently polar) or by doping to enforce cation ordering on the B site in order to produce a polar commensurate lock-in transition similar to that observed in Pb_2CoWO_6,[88] and commonly observed in the β-K_2SO_4 family of ferroelectrics[89] (e.g., K_2SeO_4).[90,91]

The electrical polarization within $Bi_2Mn_{4/3}Ni_{2/3}O_6$ is thus frustrated by competing displacements on the A and B cation sublattices. Muon spin relaxation, ac susceptibility, and dc $M(H)$ FC data show that the spins on the B site are frozen rather than long-range ordered, and thus, the targeted ferromagnetic long-range order is also suppressed. The positive Weiss constant is consistent with dominant ferromagnetic interactions (from both the $Mn^{4+}-Ni^{2+}$ exchange favored by the partial Mn/Ni site order revealed in the low-temperature incommensurate structure and also ferromagnetic Mn^{3+}/Mn^{4+} interactions seen in several charge-ordered (overall antiferromagnetic) manganates, e.g. the CE antiferromagnetic structures of $La_{1/2}Ca_{1/2}MnO_3$[92] and $Pr_{1/2}Ca_{1/2}MnO_3$, among others[94]). Ferromagnetic order is frustrated by the positional disorder resulting from the mismatch between the cation composition and the structure, and from the competing antiferromagnetic (e.g., $Ni^{2+}-Ni^{2+}$) exchange interactions that are thus produced, resulting in the observed spin-glass-like behavior. The variable-temperature low T structural data and the magnetodielectric data reveal how the local magnetization of the frozen clusters within the spin-glass-like state couples to the locally polar regions within the structure, despite the frustration of both types of long-range order. The temperature dependence of the subcell parameters shows a strong structural response, particularly along the potentially polar

(80) Schmidt, R.; Eerenstein, W.; Winiecki, T.; Morrison, F. D.; Midgley, P. A. *Phys. Rev. B* **2007**, *75*, 245111/1–245111/8.
(81) Belik, A. A.; Iikubo, S.; Yokosawa, T.; Kodama, K.; Igawa, N.; Shamoto, S.; Azuma, M.; Takano, M.; Kimoto, K.; Matsui, Y.; Takayama-Muromachi, E. *J. Am. Chem. Soc.* **2007**, *129*, 971–977.
(82) Montanari, E.; Righi, L.; Calestani, G.; Migliori, A.; Gilioli, E.; Bolzoni, F. *Chem. Mater.* **2005**, *17*, 1765–1773.
(83) Bokov, V. A.; Myl'nikova, I. E.; Kizhaev, S. A.; Bryzhina, M. F.; Grigoryan, N. A. *Fizika Tverdogo Tela* **1965**, *7*, 3695–8.
(84) Belik, A. A.; Yokosawa, T.; Kimoto, K.; Matsui, Y.; Takayama-Muromachi, E. *Chem. Mater.* **2007**, *19*, 1679–1689.
(85) Fujino, S.; Murakami, M.; Lim, S. H.; Salamanca-Riba, L. G.; Wuttig, M.; Takeuchi, I. *J. Appl. Phys.* **2007**, *101*, 013903/1−013903/3.
(86) Azuma, M.; Niitaka, S.; Belik, A.; Ishiwata, S.; Saito, T.; Takata, K.; Yamada, I.; Shimakawa, Y.; Takano, M. *Trans. Mater. Res. Soc. Jpn.* **2006**, *31*, 41–46.
(87) Moreira dos Santos, A. F.; Cheetham, A. K.; Tian, W.; Pan, X.; Jia, Y.; Murphy, N. J.; Lettieri, J.; Schlom, D. G. *Appl. Phys. Lett.* **2004**, *84*, 91–93.
(88) Buehrer, W.; Ruedlinger, M.; Maaroufi, F.; Toledano, P.; Schmid, H.; Brixel, W.; Sciau, P. *Physica B* **1989**, *156*, 10–11.
(89) Chen, Z. Y.; Walker, M. B. *Phys. Rev. B* **1991**, *43*, 5634–5648.
(90) Yamada, N.; Ikeda, T. *J. Phys. Soc. Jpn.* **1984**, *53*, 2555–2564.
(91) Yamada, N.; Ono, Y.; Ikeda, T. *J. Phys. Soc. Jpn.* **1984**, *53*, 2565–2574.
(92) Wollan, E. O. *Phys. Rev.* **1955**, *100*, 545–563.
(93) Tomioka, Y.; Asamitsu, A.; Kuwahara, H.; Moritomo, Y.; Tokura, Y. *Phys. Rev. B* **1996**, *53*, R1689–R1692.
(94) Dunaevsky, S. M.; Deriglazov, V. V. *Phys. Solid State* **2008**, *50*, 101–107.

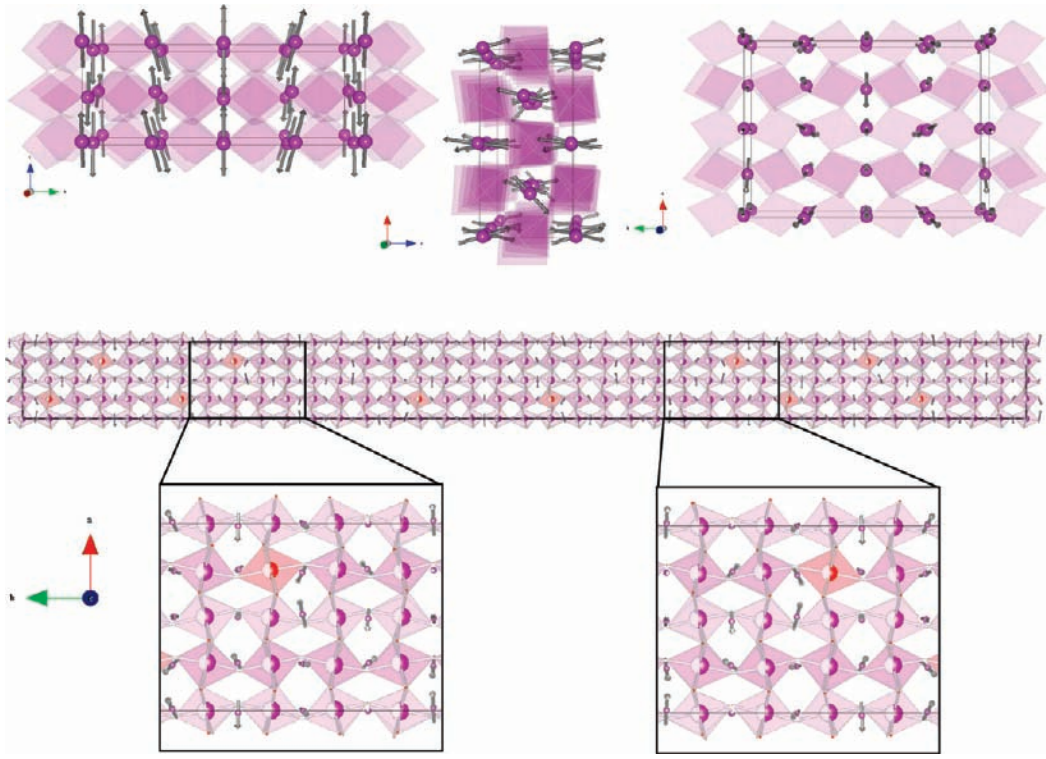

Figure 10. (Top) Short range approximant ($2\sqrt{2}a_p \times 4a_p \times \sqrt{2}a_p$) to the incommensurate structure, viewed down the three principle axes. Arrows represent Bi displacements from the centroid of the BiO_{12} environment. The polarization calculated for this approximant is 56 $\mu C/cm^2$. (Bottom) Long range approximant ($2\sqrt{2}a_p \times 38a_p \times \sqrt{2}a_p$, same origin choice as in Figure 5) viewed down the nonmodulated axis. Blue purple octahedra have >50% Mn occupancy and red octahedra >50% Ni. Arrows represent Bi displacements from the centroid of the BiO_{12} environment. Two expanded regions are shown; the mirror relationship between them reveals how the modulation suppresses the local polarization via the creation of symmetries between locally polar subcomponents.

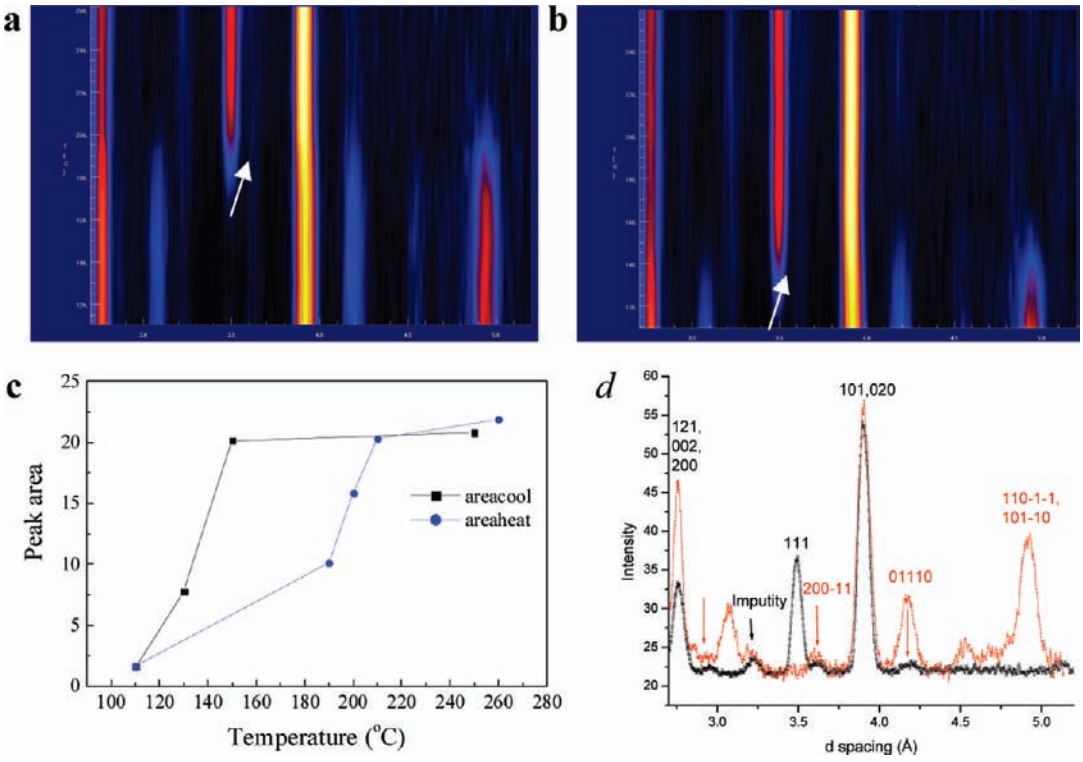

Figure 11. Neutron diffraction (GEM bank 3 $d = 2.7-5.2$ Å) showing the disapearence of the modulated peaks and the growth of a peak associated with the high temperature phase (marked with an arrow (111)) (a) on heating and (b) on cooling. (c) Integrated area under the peak (111) marked by the arrow in (a) and (b) on heating and cooling showing hysteresis. (d) 250 °C data set (black symbols) showing the remnant intensity of the modulation peaks (red arrows) the room temperature data is included for comparison (red symbols), black indices refer the high temperature cell, and red indices to the modulated structure.

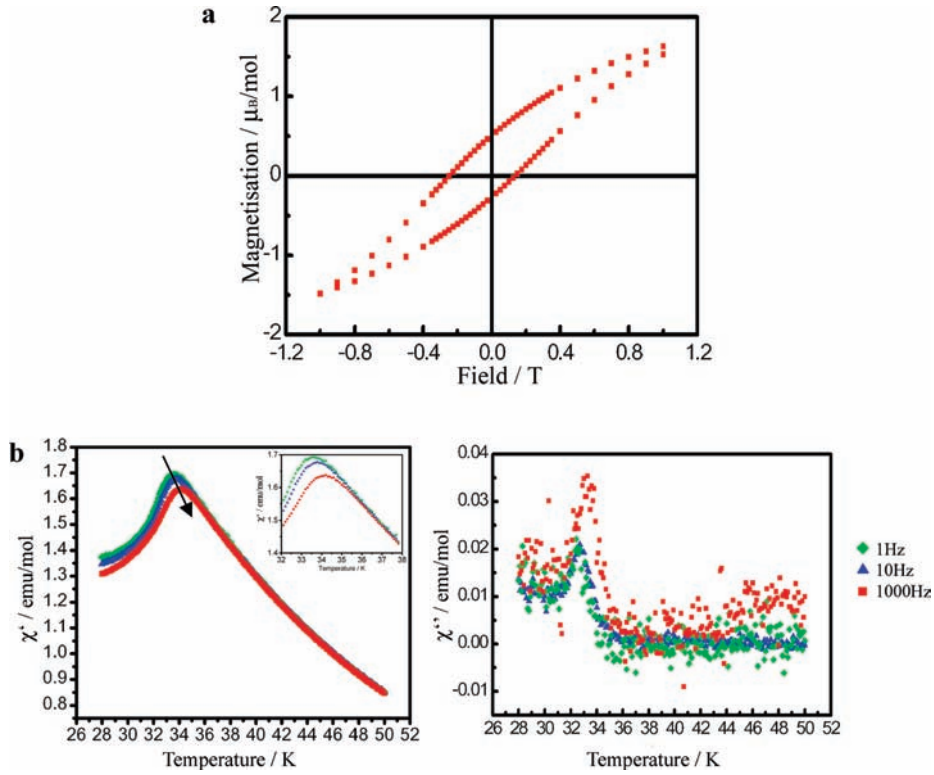

Figure 12. (a) Field dependence of the dc magnetization at 2 K collected on the crystals after cooling in a 1 T field. (b) ac Magnetic susceptibility for $Bi_2Mn_{4/3}Ni_{2/3}O_6$ for the real (left) and imaginary (right) components. The frequency dependence is consistent with spin-glass-like behavior.

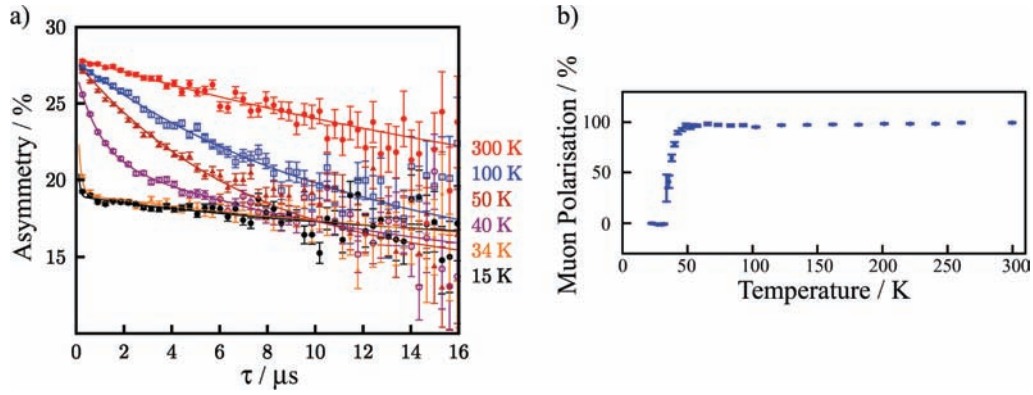

Figure 13. (a) Muon asymmetry data for a polycrystalline sample of $Bi_2Mn_{4/3}Ni_{2/3}O_6$ as a function of time for six selected temperatures. (b) The initial normalized muon polarization of $Bi_2Mn_{4/3}Ni_{2/3}O_6$ as a function of temperature (normalization has been carried out to display the percentage of muons not coupled to a static local field, therefore 0% in the frozen phase and 100% in the paramagnetic phase).

a direction, to the magnetic ordering which is confirmed by the magnetodielectric response. The shape of the magnetodielectric effect (the magnetic field dependence of the relative permittivity) is related to the existence of coupling terms in the Landau free energy $F = F(M,P)$ where M and P are the magnetic and ferroelectric order parameters. In the case of $BiMnO_3$[22] and $YMnO_3$,[58] where the important term is the one that couples quadratic polarization with quadratic magnetization, P^2M^2, produces a relative permittivity proportional to $\varepsilon \sim M^2$. Other terms appear to be more important in other oxide systems, giving a relative permittivity proportional to the magnetic susceptibility $\varepsilon \sim \chi_M$.[56,57] In $Bi_2Mn_{4/3}Ni_{2/3}O_6$ a quadratic term $\varepsilon \sim M^2$ predominates at temperatures well below T_{sg}, similar behavior has been observed for $BiMnO_3$ near T_c although whether this is due to magnetoelectric coupling or magnetoelastic strain is the subject of debate.[22,25] When the spin-glass-like transition takes place, a new order parameter appears, though unlike $BiMnO_3$ the magnetodielectric effect is not dependent on M^2,[22,25] creating a new coupling term proportional to H^2 and producing the observed more complex response shape. The order parameter of a spin-glass transition is the nonlinear magnetic susceptibility, and the details of the coupling with the local polarization require further detailed study. This change in the magnetoelectric coupling occurs at the same temperature as the subcell parameter anomalies at T_{sg}.

$Bi_2Mn_{4/3}Ni_{2/3}O_6$ is expected to have a local spontaneous polarization P on length scales intermediate between the commensurate and approximant cell sizes and also to form magnetic clusters due to the competing exchange interactions in the spin-glass state with a given magnetization M. It can be then considered as a local multiferroic, and coupling can be expected at a local scale. No macroscopic polarization is

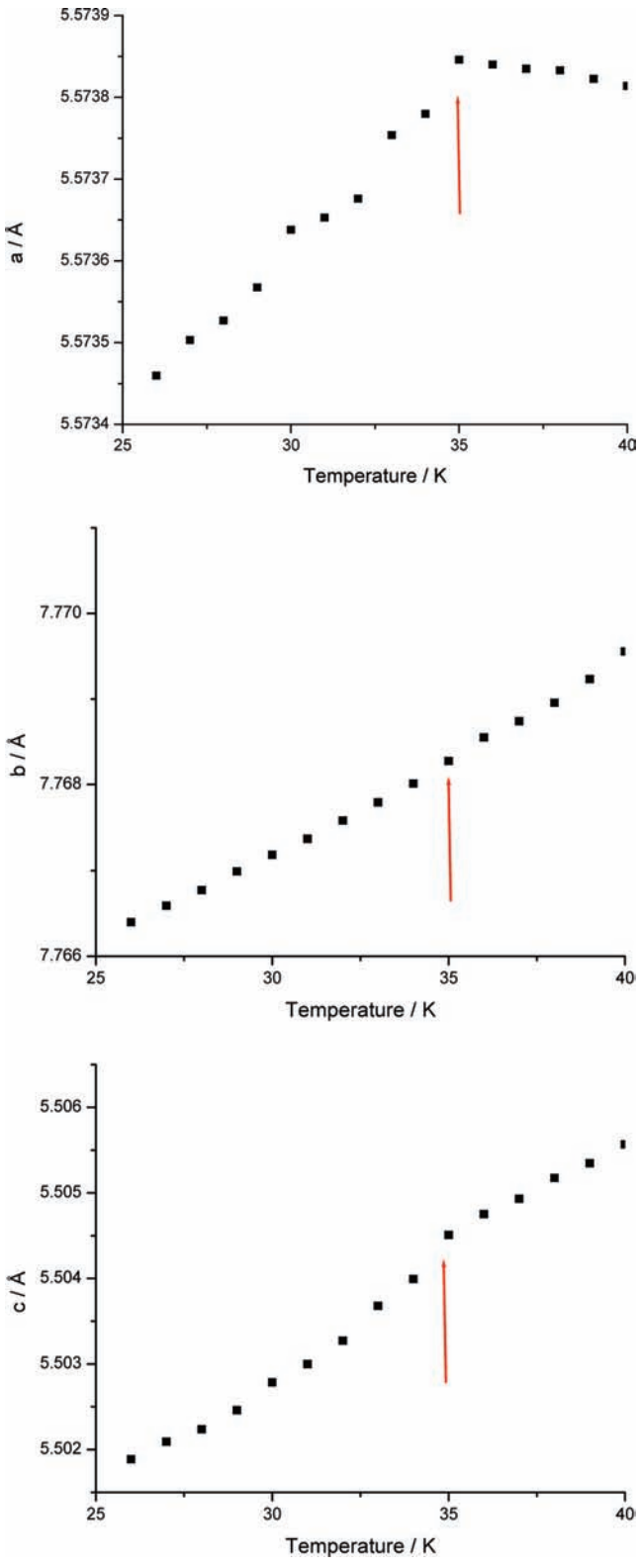

Figure 14. Variation of the subcell lattice parameters of $Bi_2Mn_{4/3}Ni_{2/3}O_6$ as a function of temperature. The arrows indicate the change in slope of the lattice parameters at 35 K close to the measured spin-glass freezing transition at 37K.

expected from the crystallographic data, so that macroscopic measurements of polarization cannot be used to evidence direct magnetoelectric coupling. However, electric susceptibility measurements are possible and do show coupling between dielectric and magnetic properties. This magnetodielectric coupling is at

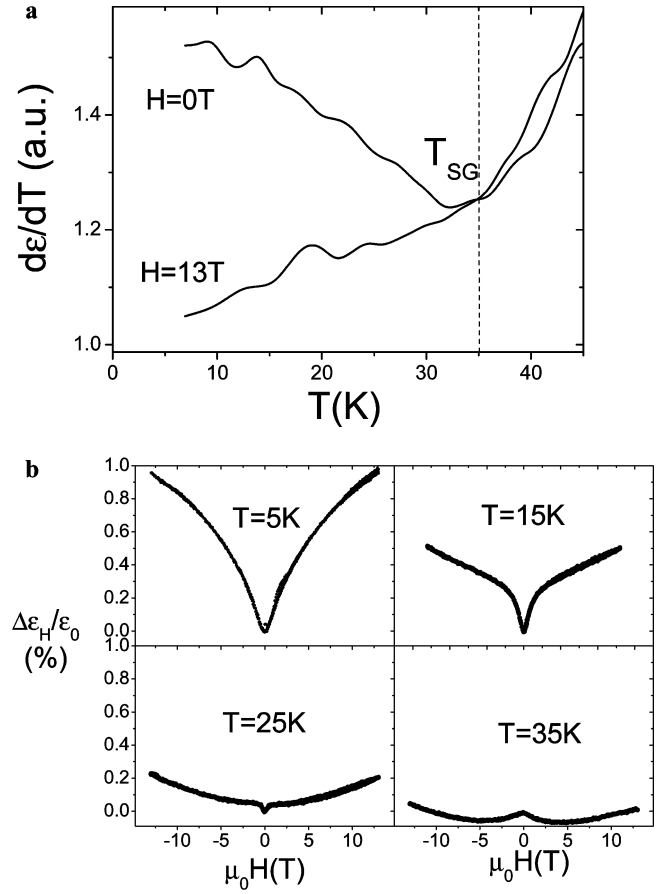

Figure 15. (a) Temperature dependence of the first derivative of the relative permittivity of $Bi_2Mn_{4/3}Ni_{2/3}O_6$ at 0 T and 13 T. An anomaly appears at the spin-glass transition which disappears under the application of 13 T. (b) Magnetodielectric effect of $Bi_2Mn_{4/3}Ni_{2/3}O_6$ at low temperature. Two different field dependences are in competition around T_{SG} as shown by the multiple minima.

the origin of the field-dependent dielectric constant behavior in our data, and further exploration of how the spin glass and modulated antiferroelectric ground states are coupled is merited to explain the novel behavior of the magnetocapacitance of $Bi_2Mn_{4/3}Ni_{2/3}O_6$.

Conclusions

$Bi_2Mn_{4/3}Ni_{2/3}O_6$ has a line phase composition which accommodates the competing structural environments of Mn^{4+}, Mn^{3+}, and Ni^{2+} on the octahedral B site with the asymmetric Bi^{3+} on the A site of the perovskite structure. The bonding flexibility permitted by the multiple B site cations allows the structural requirements of Bi on the A site of the perovskite structure to be accommodated, stabilizing a rare example of a pure Bi A site perovskite. The fraction of the different B site charge states required to stabilize Bi^{3+} does not match well with site or charge order, producing a natural structural and compositional frustration that defines both the crystal chemistry and the property coupling of this material. The interplay of the different bonding preferences of the octahedral cations seems to permit the development of a structural environment that will accommodate Bi. The multiplicity of cations on the B site operates against the development of commensurate long-range cation site order. The other potential long-range order is that of the off-center displacements of Bi^{3+} within their immediate cage of oxygen neighbors. The result of the competition between these orderings

on the B site and the A site is a modulated structure which is close to being polar; the effect of the modulation is to cancel out the local polarity of multiple perovskite unit cells in an analogue of the unit-cell scale antiferroelectric ordering of polar A site displacements in lead perovskites. The antiferroelectric Bi displacements are stable in the high *T* structure where there are only two B sites species; the electronic B site ordering at low temperature produces a more complex A site displacement pattern with large local polar regions.

The nature of the B cation appears to strongly control the nature of the A site displacements that are possible in $BiBO_3$ perovskites. In $BiFeO_3$ polar A site displacements are possible, enabled by the coordination flexibility of the d^5 Fe^{3+} ion which can adopt a range of bonding environments. In the present case, the high T structure has no long-range commensurate Mn/Ni order and permits only antipolar A site displacements. The presence of polar A site displacements over $4a_p$ distances in the low *T* structure is frustrated by the incommensurate antiferroelectric modulation on a $40a_p$ length scale to permit the Mn/Ni site order, any charge or orbital order on the B site and A site local polar displacements to coexist. Relative permittivity measurements reveal a coupling between the local polarization and the local magnetization generated by the competing exchange interactions on the partially cation ordered but multiple valence state B site. As orbital ordering energies in Mn^{3+} systems are very high, a possible frustrating role of these orbital ordering patterns on candidate polar A site displacements in $BiMnO_3$ needs to be seriously considered as the origin of the conflicting properties reported for this material and could stabilize multiple competing slightly incommensurate ground states.

Acknowledgment. We acknowledge the UK EPSRC for support under EP/C511794 and for access to SRS (where Dr. M. A. Roberts is thanked for assistance on beamline 9.1), ISIS (where Dr. W. Koeckelmann is thanked for assistance on the GEM diffractometer) and ILL (where Dr. P. F. Henry is thanked for assistance on the D2B and D20 diffractometers.). We additionally acknowledge support from the FAME Network of Excellence under the EU Framework VI programme and the STREP MaCoMuFi (NMP3-CT-2006- 033221) supported by the European Community and by the CNRS, France. N.B. acknowledges financial support to NOVELOX ESRT MEST-CT-2004-514237 and CNRS. P.S.H. thanks the Welch Foundation (Grant E-1457), NSF (DMR-0652150), and ACS PRF (47345-AC10) for support.

Supporting Information Available: Ten additional figures and two tables together with the final powder neutron refinement. This material is available free of charge via the Internet at http://pubs.acs.org.

JA902424X